UNIVERSITAT POLITÈCNICA DE VALÈNCIA

SAPIENZA, UNIVERSITÀ DI ROMA

LAUNCH VEHICLE ATTITUDE CONTROL IN ATMOSPHERIC FLIGHT

Bachellor's Thesis

Aerospace engineering

AUTHOR: Beatriz Gironés Sangüesa

Tutor: Sergio García-Nieto Rodríguez

External tutor: Guido De Matteis

External cotutor: Alessandro Zavoli

ACADEMIC YEAR: 2018-2022

Abstract

The thesis describes the development of control methods for attitude control during the atmospheric flight of a launch vehicle (LV).

In order to solve the attitude control problem, a mathematical model of the dynamics of the launch vehicle is first defined. The linearized equations of motion are then derived under the assumption that the vehicle will experience only small deviations from a reference trajectory. One of the main concerns during the modelling is comprising the structural load caused by wind gusts. The atmospheric phase of flight is a difficult scenario for launch vehicles.

The control system must be capable of providing stability margins under demanding conditions while also ensuring performance and robustness. A baseline controller (BC) with two proportional-derivative (PD) components for attitude and translational motion control is created using the time-invariant linear model.

The controller design focused on the LV rigid motion is based on traditional control theory. Two pole placement methods are used attending to old techniques inside control systems. In this way, the controller is designed by a manual gain search and a LQR technique. The controller prototypes are simulated with Matlab and Simulink during the whole process.

It is finally deduced that the biggest constrain in the work is to balance performance with robustness found in stability. Moreover, the traditional processes are found to be time-consuming and challenging with respect to accuracy in the response.

Contents

List of Figures

1 Introduction

1.1 Project outline

The thesis describes the design process of a launch vehicle's (LV) control system in order to fly a prescribed trajectory. This project focuses only on the atmospheric flight stages, starting at liftoff, going through the first stage separation and analysing a small period of flight time. The system covers attitude control through a single input, the Thrust Vector Control (TVC) angle which deflects to orientate the vehicle in the desirable direction.

A TVC system is commonly used to control the pitch and yaw axes of the atmospheric stage [1]. The launcher flight control system calculates the necessary engine nozzle deflections to guarantee stability and comply with the orders on prescribed attitude angles based on the measurements from the Inertial Navigation System (INS).

When designing a rocket, one of the most important criteria to consider is stability. Apart from attaining high speeds during launch, it must maintain its orientation and desired flight plan to avoid wobbling and tumbling. Stability can be achieved either by structural elements such as fins, or by modifying the control system. The last one is specifically the aim of this project.

One of the mayor concerns is that launch vehicles are aerodynamically unstable by nature, as the center of gravity is located behind the center of pressure. Moreover, density changes through the atmospheric layers, which affects the dynamic pressure. At its maximum point, aerodynamic loads could damage the structural integrity of LV and can result in severe performance loss of the vehicle [2]. The report has concentrated in studying the behaviour in this area in order to work with the most critical condition.

Another challenge that has to be faced with LV design is its flexible dynamics. The initial bending modes' frequency range typically are somewhat near to the rigid body dynamics' frequency range, making the vehicle dynamics unstable. [3]

Hence, it is necessary to design a controller paying close attention to the aspects mentioned above.

The controller may be designed with classical control systems such as the traditional PID control and the Linear Quadratic Regulator (LQR) controller. These methods have been used in real space projects like the Ares-I launch vehicle [4]. Classical control systems, such as PID controllers with gain scheduling, are often capable of meeting flight requirements and stability and performance standards, as well as other flight certification parameters. However, they have several practical constraints. The main disadvantage is that the procedure is extremely time consuming, owing to the difficulty of addressing a multivariable problem while attempting to ensure robustness [5].

1.2 Objectives

The purpose of this work is the appropriate design of a Flight Control System (FCS) of a launch vehicle, regarding attitude control. Typically, the attitude control problem is focused with the vehicle's short-period dynamics.

The primary goal is to maintain the systems stability, achieve an appropriate response to guiding orders while resisting wind disturbances (wind gusts), restricting aerodynamic loads and minimizing deviation from a reference trajectory. In addition, stability margin requirements impose the robustness features.

The controller is designed with two different approaches inside the pole placement method. The application of manual gain search and LQR techniques is proposed to overcome the current challenges of system.

Once the controller is built, it is wanted to analyze the limitations of the traditional control systems. It will be studied the efficiency in the design process, such as gain tuning and the performance achieved by each method.

To sum everything up, the most important subject is to accomplish stability regarding the aerodynamic instability of the LV and its flexible dynamics, and increase performance, achieved by aerodynamic load minimization and trajectory error minimization.

1.3 Thesis structure

Chapter 2 presents the first step in the FCS design, the system modelling. To facilitate the subsequent calculations the simplest mathematical model should be developed. In the thesis the Greensite model [6] is taken as reference, which offers enough precision for the current work. In addition to the model of the system itself, the simulation of other dynamic elements should also be taking into account such as TVC actuator, delay and sensors.

Afterwards, in Chapter 3 the attitude control system is designed in various stages. An autopilot configuration that meets design requirements is searched for, also considering a linear system to study the short-period dynamics. A proportional and derivative (PD) controller is proposed for the pitch axis to decrease lateral deviations, and a PD controller is selected for the drift channel.

The full design of this control is defined in Chapter 4. A rigid-body controller based on a PD controller is employed to provide pitch and yaw axis stabilisation. Feedback loops are included in every state to reduce the structural loads on the launch vehicle. The design is developed in two different methods; manual pole placement and Linear Quadratic Regulator (LQR) controllers.

Chapter 5 presents the final results obtained from both controllers. The outcomes are compared and their efficiency are analyzed.

Finally, Chapter 6 describes the important accomplishments of the project as well as proposes ideas for a possible improvement in the future.

2 Launch Vehicle Modeling

This section describes the mathematical model of the LV during the atmospheric phase of flight. It will be considered rigid body and flexible dynamics for the systems modelling. Moreover, a wind model representing the possible disturbances that wind gusts can create during the phase of flight is considered.

2.1 LV model

The LV attitude is modelled with 6 DoF equations of motion. The equations are obtained from [6].

In order to simplify the design, pitch and yaw axes are assumed to be decoupled. This can be considered as the LV is symmetric about the roll axis and the roll rate is usually low enough. In this way, the motion is reduced to a 3 DoF linear model. Two reference frames are taken into account, that is, the dynamics of the vehicle are expressed by a body-fixed frame (X_b, Z_b) with respect to a set trajectory at a reference frame (X_t, Z_t). The modeling can be divided considering the following features:

- Rigid-body translation and rotation
- Structural elastic dynamics in terms of bending modes
- Aerodynamic and propulsive force and moments
- TVC actuators dynamics

2.1.1 Rigid-body model

The linear dynamic model is defined in two dimensions [7] regarding attitude. The motion is described as a body (body frame **B**) following an ascent trajectory (non-stationary frame **T**). The scheme is illustrated in Fig. 1.

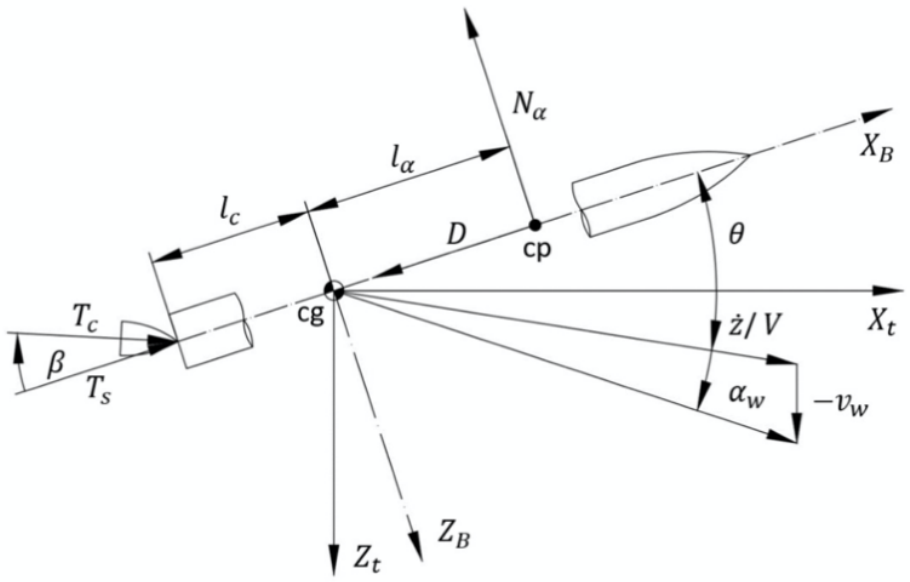

Figure 1: Sketch of a rigid LV model

The frame that is attached to the body S_B is a right-hand coordinate system, X_B, Y_B, and Z_B fixed to the vehicle body having basis vectors $\hat{i}$, $\hat{j}$, $\hat{k}$. The $\hat{i} - axis$ is parallel to the vehicle's longitudinal axis pointing, the $\hat{j} - axis$ points downward and the $\hat{k} - axis$ points rightward.

The reference frame for the trajectory S_t is a right-hand non-stationary frame with basis vectors $\hat{i}_t$, $\hat{j}_t$, $\hat{k}_t$ and coordinates X_t, Y_t, Z_t that moves axially with the vehicle while remaining tangent to the ascent trajectory. $\hat{i}_t$ and $\hat{j}_t$ axes are tangent and normal to the nominal trajectory, respectively. And $\hat{k}_t$ is orthogonal to both of them..

In this way, the equations for the rigid body are the following:

$$\ddot{\theta} = \frac{N_\alpha l_\alpha}{I_{yy}}\theta + \frac{N_\alpha l_\alpha}{I_{yy}V}\dot{z} + \frac{T_c l_c}{I_{yy}}\beta - \frac{N_\alpha l_\alpha}{I_{yy}}\alpha_\omega \tag{1}$$

$$\ddot{z} = \frac{D - T_t - N_\alpha}{m}\theta - \frac{N_\alpha}{mV}\dot{z} + \frac{T_c}{m}\beta + \frac{N_\alpha}{m}\alpha_\omega \tag{2}$$

$$\alpha = \theta + \frac{\dot{z}}{V} - \alpha_\omega \tag{3}$$

where θ is the perturbed pitch angle relative to the trajectory frame, α is the angle of attack, z is the drift position of the center of mass c.g with respect to the reference trajectory frame and $\dot{z}$ the related drift velocity, m is the LV mass, $T_t = T_s + T$ is the total thrust force composed of the sustained thrust T_s and the control (swiveled) thrust T_c. Finally, N_α is the aerodynamic normal force acting on the center of pressure, D is the aerodynamic axial force (drag), β the nozzle rotation angle, V the forward velocity of the vehicle, $\alpha = \frac{V_\omega}{V}$ is the wind-induced angle of attack and V_ω is the wind disturbance velocity.

Eqs. 1 and 2 can be simplified defining the following parameters:

$$A_6 = \frac{N_\alpha l_\alpha}{I_{yy}} \qquad K_1 = \frac{T_c l_c}{I_{yy}} \qquad a_1 = -\frac{N_\alpha}{mV} \qquad a_3 = \frac{T_c}{m} \qquad a_4 = -\frac{(T_t - D)}{m} \tag{4}$$

where A_6 and K_1 are known as aerodynamic and control moment coefficient respectively.

2.1.2 Flexible Body Dynamics

The LV can be assumed as quasi-rigid. The elastic DoFs are detailed to complete the vehicle model, and the modal decomposition method [6] is used to do so.

Some simplifications can be made taking into account that the LV model has a relatively constant cross-section along its length with no important aerodynamic features (fins, wing, etc.) and controlled by TVC with a nozzle positioned at the base of the rocket. The bending modes are uncoupled from the rigid motion and are exited by the inertial effects of engine thrust and nozzle rotation, while aerodynamic effects are ignored. [3]

In Fig. 2, relevant variables representing flexible dynamics are illustrated, with a simplified schematic of the deflected form of the LV. It is shown the elastic deflection $\xi(x,t)$, the nozzle longitudinal coordinate x_G, and the thrust control force T_c. [8]

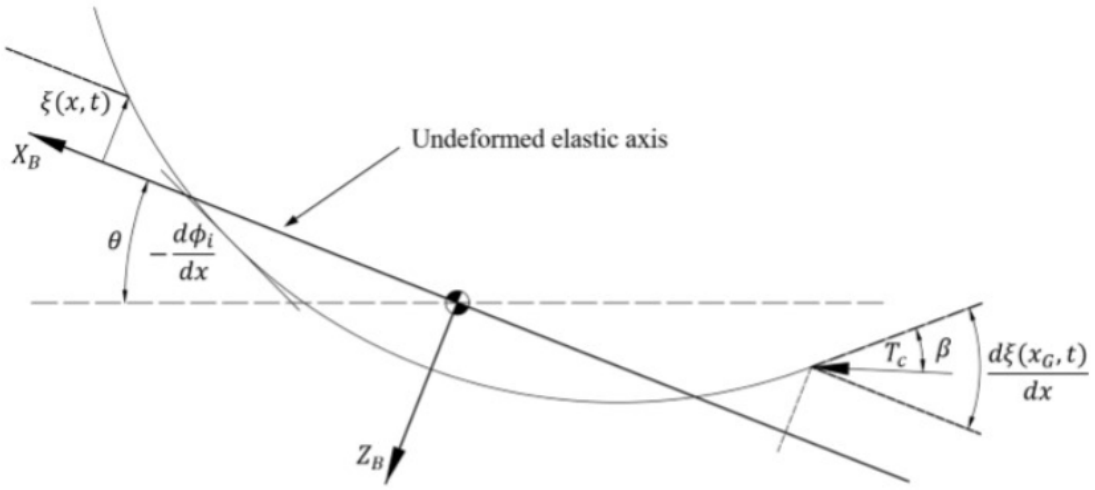

Figure 2: Sketch of a flexible LV model

The elastic deflection in relation to the body frame at any position along the vehicle is given by:

$$\xi(x,t) = \sum_{i=1}^{\infty} \phi_i(x) q_i(t) \tag{5}$$

where x is the abscissa along the LV longitudinal axis, ϕ_i is the normalized mass of the $i-th$ mode shape in the pitch plane, and q_i is the $i-th$ mode's generalized coordinate. Several resonant modes describe the LV flexible nature. The following 2nd order model with natural frequency ω_i and damping ratio ζ_i represents the dynamics of the $i-th$ mode:

$$\ddot{q}_i + 2\zeta\omega_i\dot{q}_i + \omega_i^2 q_i = -Q_i \tag{6}$$

where Q_i is the generalized force due to the moments and normal forces acting on the LV. It can be expressed as:

$$Q_i = \int_0^L (\sum F_z \phi_i(x) + \sum M_y \sigma_i(x)) dx \tag{7}$$

being the modal rotation σ

$$\sigma_i = -\frac{\partial \phi_i}{\partial x} \tag{8}$$

F_z (normal force) and M_y (moment) may be caused by gravity, aerodynamics, propulsion, and nozzle inertia, albeit only the thrust component is considered for the purposes of this study. As a result, Eq. 6 becomes:

$$\ddot{q}_i + 2\zeta\omega_i\dot{q}_i + \omega_i^2 q_i = -T_c \phi_i \beta \tag{9}$$

2.1.3 State Space representation

The prior motion equations allow the LV model to be represented in state-space form, which is more suited for analysis and design of the later flight control system.

$$\ddot{x} = A\mathbf{x} + B\mathbf{u} \tag{10}$$

$$y = C\mathbf{x} + D\mathbf{u} \tag{11}$$

The state vector includes the rigid body variables and the first bending mode:

$$\mathbf{x} = [\theta \quad \dot{\theta} \quad z \quad \dot{z} \quad q \quad \dot{q}] \tag{12}$$

The input to the system is the TVC rotation angle β and the wind induced angle of attack α_ω given by the input vector:

$$\mathbf{u} = [\beta \quad \alpha_\omega] \tag{13}$$

and the governing equations are then written in matrix form, from Eqs. 1,2,3, 9,as:

$$\dot{x} = \begin{bmatrix} \dot{z} \\ \ddot{z} \\ \dot{\theta} \\ \ddot{\theta} \\ \dot{q} \\ \ddot{q} \end{bmatrix} = \begin{bmatrix} 0 & 1 & 0 & 0 & 0 & 0 \\ 0 & -\frac{N_\alpha}{mV} & \frac{D-T_t-N_\alpha}{m} & 0 & 0 & 0 \\ 0 & 0 & 0 & 1 & 0 & 0 \\ 0 & \frac{N_\alpha l_\alpha}{I_{yy}V} & \frac{N_\alpha l_\alpha}{I_{yy}} & 0 & 0 & 0 \\ 0 & 0 & 0 & 0 & 0 & 1 \\ 0 & 0 & 0 & 0 & -\omega_{BM}^2 & -2\zeta_{BM}\omega_{BM} \end{bmatrix} \begin{bmatrix} z \\ \dot{z} \\ \theta \\ \dot{\theta} \\ q \\ \dot{q} \end{bmatrix} + \begin{bmatrix} 0 \\ \frac{T_c}{m} \\ 0 \\ \frac{T_c l_c}{I_{yy}} \\ 0 \\ -\hat{\phi}_{TVC} T_c \end{bmatrix} \beta + \begin{bmatrix} 0 \\ \frac{N_\alpha}{m} \\ 0 \\ -\frac{N_\alpha l_\alpha}{I_{yy}} \\ 0 \\ 0 \end{bmatrix} \alpha_\omega \tag{14}$$

Finally, the output vector considers the inertial navigation system measurements as:

$$y = \begin{bmatrix} z_{INS} \\ \dot{z}_{INS} \\ \theta_{INS} \\ \dot{\theta}_{INS} \end{bmatrix} = \begin{bmatrix} 1 & 0 & 0 & 0 & -\phi_{INS} & 0 \\ 0 & 1 & 0 & 0 & 0 & -\phi_{INS} \\ 0 & 0 & 1 & 0 & \sigma_{INS} & 0 \\ 0 & 0 & 0 & 1 & 0 & \sigma_{INS} \end{bmatrix} \begin{bmatrix} z \\ \dot{z} \\ \theta \\ \dot{\theta} \\ q \\ \dot{q} \end{bmatrix} \tag{15}$$

where ϕ_{INS} is the bending mode displacement and σ_{INS} is the rotation, both at the location of the Inertial Navigation System (INS).

This sensor provides information regarding the vehicle rotation and rotation rate, as well as translation sensing. In this way, local elastic disturbances are also taken into account.

In this report, the FCS only takes into account rigid body motion. Thus, the state space representation ignoring flexible dynamics becomes:

$$\dot{x} = \begin{bmatrix} \dot{z} \\ \ddot{z} \\ \dot{\theta} \\ \ddot{\theta} \end{bmatrix} = \begin{bmatrix} 0 & 1 & 0 & 0 \\ 0 & -\frac{N_\alpha}{mV} & \frac{D-T_t-N_\alpha}{m} & 0 \\ 0 & 0 & 0 & 1 \\ 0 & \frac{N_\alpha l_\alpha}{I_{yy}V} & \frac{N_\alpha l_\alpha}{I_{yy}} & 0 \end{bmatrix} \begin{bmatrix} z \\ \dot{z} \\ \theta \\ \dot{\theta} \end{bmatrix} + \begin{bmatrix} 0 \\ \frac{T_c}{m} \\ 0 \\ \frac{T_c l_c}{I_{yy}} \end{bmatrix} \beta + \begin{bmatrix} 0 \\ \frac{N_\alpha}{m} \\ 0 \\ -\frac{N_\alpha l_\alpha}{I_{yy}} \end{bmatrix} \alpha_\omega \tag{16}$$

$$y = \begin{bmatrix} z_{INS} \\ \dot{z}_{INS} \\ \theta_{INS} \\ \dot{\theta}_{INS} \end{bmatrix} = \begin{bmatrix} 1 & 0 & 0 & 0 \\ 0 & 1 & 0 & 0 \\ 0 & 0 & 1 & 0 \\ 0 & 0 & 0 & 1 \end{bmatrix} \begin{bmatrix} z \\ \dot{z} \\ \theta \\ \dot{\theta} \end{bmatrix} \tag{17}$$

with the state vector only including the corresponding rigid body variables:

$$\mathbf{x} = [\theta \quad \dot{\theta} \quad z \quad \dot{z}] \tag{18}$$

2.2 TVC Actuator Dynamics

Thrust Vectoring Control, or TVC, is used to give the required nozzle deflection angle for the desired thrust orientation to drive the vehicle. The actuator dynamics of the TVC system are relatively complex and non-linear. [1]

Before sending the control signal, the system is coupled in series with a delay model to account for the time delay imposed by the hardware. A second order Padé approximation is used to approximate the time delay of $\tau = 20\ ms$ caused by hardware processing times. [9]

$$\begin{bmatrix} \dot{d} \\ \ddot{d} \end{bmatrix} = \begin{bmatrix} 0 & 1 \\ -\frac{12}{\tau^2} & -\frac{6}{\tau} \end{bmatrix} \begin{bmatrix} d \\ \dot{d} \end{bmatrix} + \begin{bmatrix} 0 \\ -\frac{12}{\tau^2} \end{bmatrix} \beta_c \tag{19}$$

$$\beta_{\hat{c}} = \dot{d} + \beta_c \tag{20}$$

Where β_c and $\beta_{\hat{c}}$ are respectively, the TVC command and the same signal with delay.

The transfer function of the TVC dynamics is:

$$W_{TVC} = \frac{\beta}{\beta_{\hat{c}}} = \frac{\omega_{TVC}^2}{s^2 + 2\zeta_{TVC}\omega_{TVC}s + \omega_{TVC}^2} \tag{21}$$

where ζ_{TVC} and ω_{TVC} are the damping ration and natural frequency.

2.3 Wind Model

In this study the perturbations generated by the wind will be modelled through two different wind gust models.

2.3.1 Deterministic gust generator

The system is stressed with a synthetic step-like wind gust of the form:

$$v_\omega(t) = \begin{cases} V_a(\frac{t}{t_a})^2 & for \quad 0 \leq t < t_a \\ (V_b - V_a)\frac{t-t_a}{t_b-t_a} + V_a & for \quad t_a \leq t \leq t_b \\ V_b e^{\frac{t-t_b}{t_f-t_b}\log\frac{0.1}{|V_b|}} & for \quad t_b < t \leq t_f \end{cases} \tag{22}$$

where $t_f = 100s$, $t_a = 70s$, $t_b = 75s$, $V_a = 5m/s$ and $V_b = -30m/s$.

Fig. 3 is the plot of the previous piece-wise function characterized by:

- $t = [0, 45[$: a parabolic profile with wind velocity stating from rest to 2.5 m/s.
- $t = [45, 50[$: a linear profile with wind velocity from 2.5 to -30 m/s.
- $t = [50 - 100]$: an exponential profile with magnitude from -30 m/s to rest.

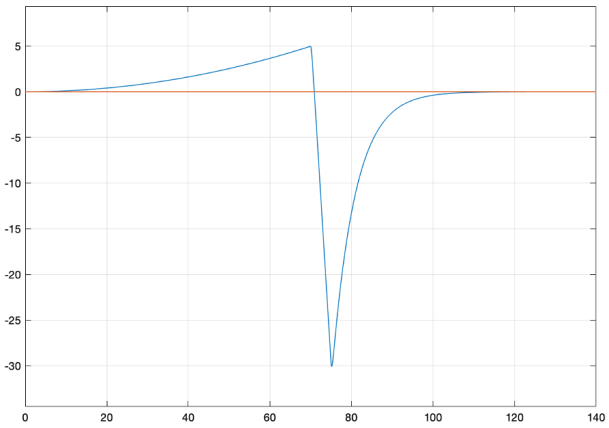

Figure 3: Deterministic step-like wind gust profile 1

It may be highlighted that in this wind gust, speed starts from a resting position and ends in the same condition. This will give considerably stable results on the performance of drift and pitch angle. For that reason, experiments will also be conducted using another wind gust which does not return to equilibrium in order to analyze more critical conditions (Fig. 4).

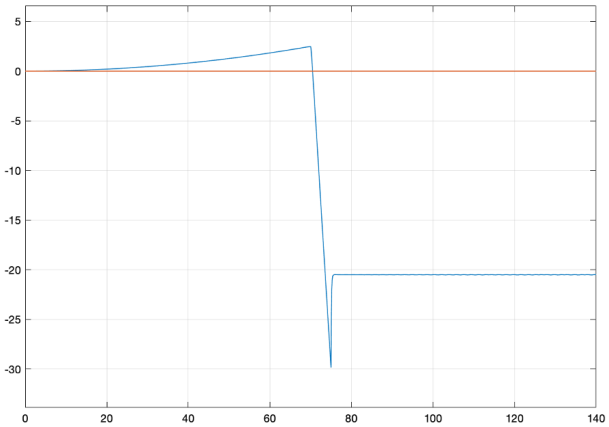

Figure 4: Deterministic step-like wind gust profile 2

2.4 Time domain Model

This system is inherently time-varying, so the transfer functions are computed at successive time-points along the trajectory. An assumption is made that stability can be assessed by considering points on the trajectory where the parameters are varying "slowly enough" that they may be assumed constant.

The time-varying model is implemented by altering the linear model parameters with time using a planned look-up table in order to explain the perturbed motion around the reference trajectory of the LV during the time span of ascending flight.

The reference LV model used in this work represents a medium-sized vehicle (lift-off mass 120.000 kg) in the same payload class as VEGA, with a complete description available in Ref. [10].

Fig. 5 depicts variations in the main LV parameters, namely A_6, K_1, and ω_{BM}, as a function of flight duration for a sample ascent trajectory from the launch pod to an altitude of 60 km.

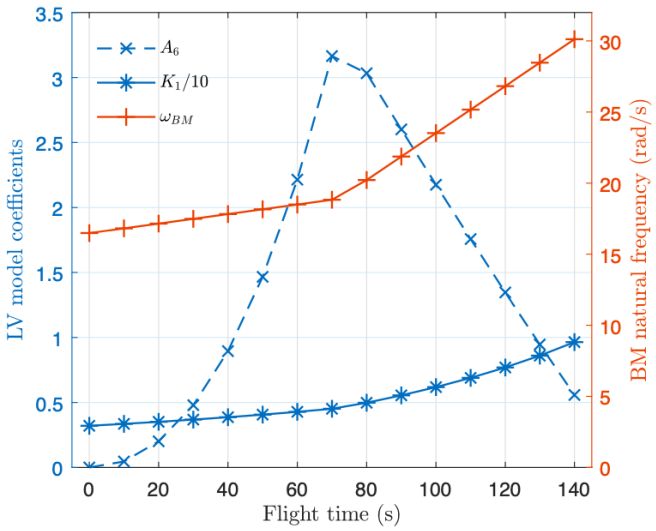

Figure 5: Aerodynamic and control moment coefficients, and bending mode natural frequency vs. flight time. [11]

Table 1 shows the whole set of model data at the highest dynamic pressure (max-Q) condition (t = 72 s).

	Unit	**Value**
m	kg	7.38×10^4
l_α	m	10.39
l_c	m	9.38
I_{yy}	kgm^2	3.28×10^6
V	m/s	937.70
Alt	m	15143
T_c	N	1.52×10^6
$T_t - D$	N	1.71×10^6
N_α	N/rad	1.07×10^6
A_6	$1/s^2$	3.3818
K_1	$1/s^2$	4.5647
a_1	$1/s^2$	-0.0154
a_3	$1/s^2$	20.6090
a_4	$1/s^2$	-27.2710
ω_{BM}	rad/s	18.9
ζ_{BM}	$-$	0.005
ϕ_{INS}	$-$	0.8
σ_{INS}	rad/m	0.178
$\hat{\phi}_{TVC}$	$1/kg$	4.31×10^{-5}
ω_{TVC}	rad/s	70
ζ_{TVC}	$-$	0.7

Table 1: LV model parameters at t=72 s (max-Q condition)[11]

3 Baseline Controller

In this section, the goal is to analyse a flight control system for the LV.

In the design of attitude control it is necessary to limit trajectory deviations in terms of attitude error and lateral drift, as well as the angle of attack, in order to ensure the structural integrity of the vehicle. The LV is stabilized by acting on TVC nozzle deflections. It is considered that the LV's motion comprises of tiny deviations from the reference trajectory.

Due to the time-invariant condition described in Subsection 2.4, to deal with rapidly changing dynamics, a gain-scheduling strategy is typically used, which involves interpolating between a series of linear controllers developed for a distinct set of LV linear models associated with numerous operational locations along the climb trajectory. The autopilot can be designed with time-varying solutions that are frozen at short periods of time. During this report, the calculus are developed only in the most critical condition of flight, during the maximum dynamic pressure stage (Table 1).

3.1 Control requirements

The flight control system must guarantee that the behaviour fulfills demanding stability and performance requirements in the face of external disturbances such as wind and parametric dispersion, in order for the system to be resilient.

The classical FCSs of LVs allow performance evaluation using classical frequency-domain criteria based on stability margins and time-domain simulations, which represent well-proven flight certification practices.

Traditional stability criteria borrowed from classical control theory, such as phase-margin and gain-margin, can be applied to the derived linear model.

Table 2 shows a group of stability requirements used for the VEGA launcher [12], set as a reference in the thesis.

	Rigid body margins			**Flexible body margins**	
	Aero GM	Rigid DM	Rigid GM	Flex GM	Flex DM
Nominal conditions	≥ 6 dB	≥ 100 ms	≤ -6 dB	≤ -3 dB	≥ 50 ms

Table 2: VEGA Stability requirements

Other than stability, performance should also be taken into account. The objective is to follow a determined trajectory, thus some boundaries are defined in Table 3 creating a margin of error in the execution.

Requirements	**Metrics**	**Bounds**
Aerodynamic load	$Q\alpha$	$< Q\alpha$ safety envelope
Lateral drift	z_{max}	< 500 m
Lateral rate drift	$\dot{z}_{max}$	< 15 m/s
TVC angle deflection	β_{max}	< 6 deg

Table 3: VEGA Performance requirements

The autopilot is designed to fulfil the established requirements, presented in the above Tables, to minimize trajectory error and aerodynamic load in order to avoid the loss of the vehicle while encountering external disturbances.

3.2 Short-period stabilization

The first need of FCS for LV stabilization is met by a PD controller on the attitude feedback channel, whose design takes into account the vehicle's rotational dynamics. Derived from Eq. 1 while ignoring wind lateral, TVC, and bending mode dynamics,

$$\ddot{\theta} = A_6\theta + K_1\beta \tag{23}$$

it is then obtained the transfer function relating θ and β

$$\frac{\theta(s)}{\beta(s)} = G(s) = \frac{K_1}{s^2 - A_6} \tag{24}$$

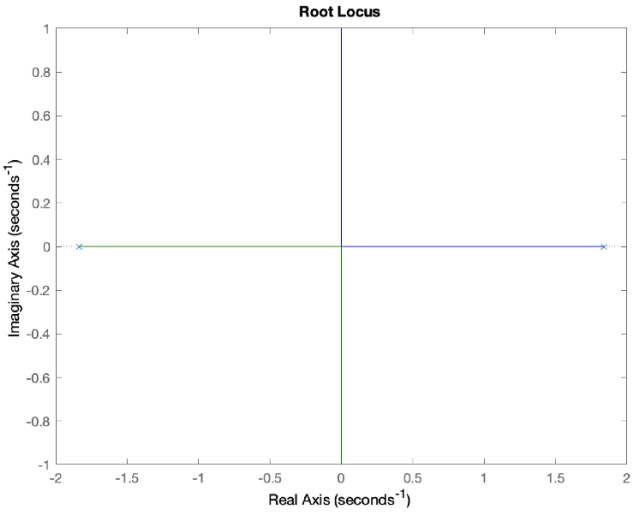

Figure 6: Rigid body pole location

Fig. 6 shows the system's root locus, where it is shown the position of the poles at $\pm\sqrt{A_6}$. The instability of the system is represented, as a branch is located in the right-half plane.

For its stabilization, it is proceeded to the design of a PD controller of the form

$$K(s) = K_{P_\theta} + K_{D_\theta}s \tag{25}$$

Considering the stability margins requirements of Table 2, K_{P_θ} and K_{D_θ} are calculated adjusting to:

- 6 dB GM at low frequency
- 30 deg PM at high frequency

$$K(s)G(s) = \frac{K_1(K_{P_\theta} + K_{D_\theta}s)}{s^2 - A_6} \tag{26}$$

At low frequency ($\omega \to 0$) it is imposed a value of 6 dB (= 2 in rad/s) gain margin, knowing that

$$s = j\omega \tag{27}$$

we can substitute in Eq. 26

$$K(j\omega)G(j\omega) = \frac{K_1(K_{P_\theta} + K_{D_\theta} j\omega)}{-\omega^2 - A_6} \tag{28}$$

obtaining for $\omega \to 0$:

$$K_{P_\theta} = \frac{2A_6}{K_1} \tag{29}$$

At high frequency, a 30 deg phase margin is considered so that

$$K(j\omega)G(j\omega) = \frac{K_1(K_{P_\theta} + K_{D_\theta} j\omega)}{-\omega^2 - A_6} = \cos 30 + j \sin 30 = (-\frac{\sqrt{3}}{2} + 0.5j) \tag{30}$$

It can be separated now the real part as

$$K_1 K_{P_\theta} = -0.866(-\omega^2 - A_6) \tag{31}$$

and knowing the value of K_{P_θ}, the frequency value can be extracted

$$\omega = \sqrt{1.31 A_6} \tag{32}$$

On the other hand, the imaginary part gives

$$K_1 K_{D_\theta} \omega = 0.5(-\omega^2 - A_6) \tag{33}$$

$$K_{D_\theta} = \frac{\sqrt{A_6}}{K_1} \tag{34}$$

In this way, the PD controller calculated will be the following:

$$K(s) = K_{P_\theta} + K_{D_\theta} s = \frac{2A_6}{K_1} + \frac{\sqrt{A_6}}{K_1} s \tag{35}$$

Fig. 7 shows the root locus once the PD controller has been applied to the system. The zero from the derivative term forces the unstable pole branch to finish at the left-half plane. Stability is then achieved.

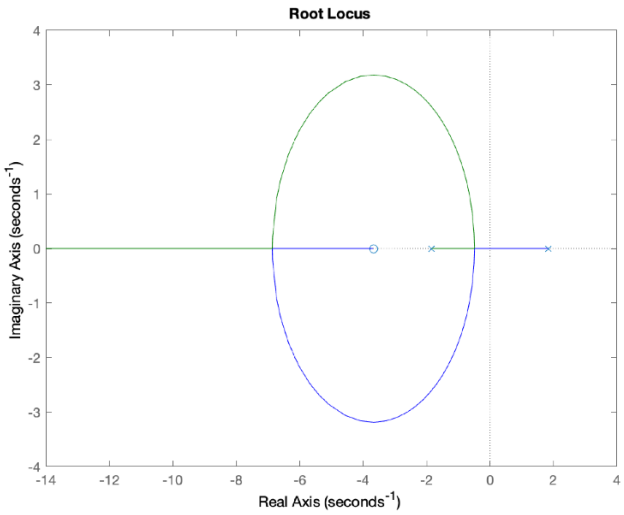

Figure 7: $K(s)G(s)$ root locus

Fig. 8, illustrates the comparison between the open-loop system $G(s)$ and the controlled system $K(s)G(s)$ at $t = 72s$. It is observed how the application of a PD controller improves gain and phase margin, as the curve is moving upwards and to the right.

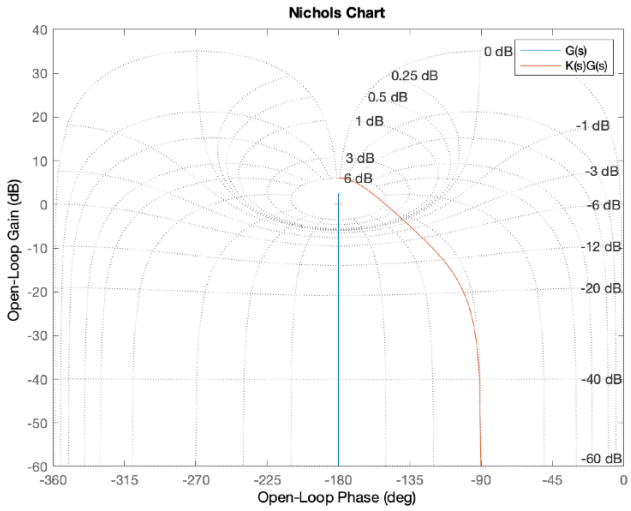

Figure 8: Nichols plots of open-loop system $G(s)$ (blue line) and controlled system $K(s)G(s)$ (orange line)

Fig. 9, shows that the stability requirements are obtained with an Aero gain margin of 6.02 dB at $\omega = 0$ rad/s and a Rigid phase margin of 29.7 deg at $\omega = 2.1$ rad/s.

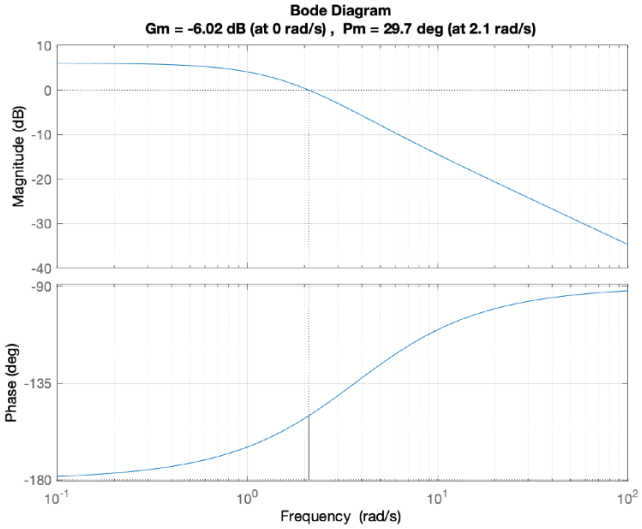

Figure 9: Bode diagram of the controlled system $K(s)G(s)$

3.3 TVC actuator dynamics

The TVC frequency response is a second-order low-pass filter that, when used in an open-loop system, has the effect of attenuating high-frequency noise and neglecting high-frequency dynamics. More crucially, the rigid body phase margin is proportional to the delays imposed by various control loop elements. As a result of the sensor dynamics, filters, and delays provided by digital computing, the phase margin and the delay margin are further deteriorated.

From the bode diagram (Fig. 10), it is seen how the phase margin has experienced a decrease of 2.4 deg, going under the stability margins, while the change in the aero gain margin can be neglected.

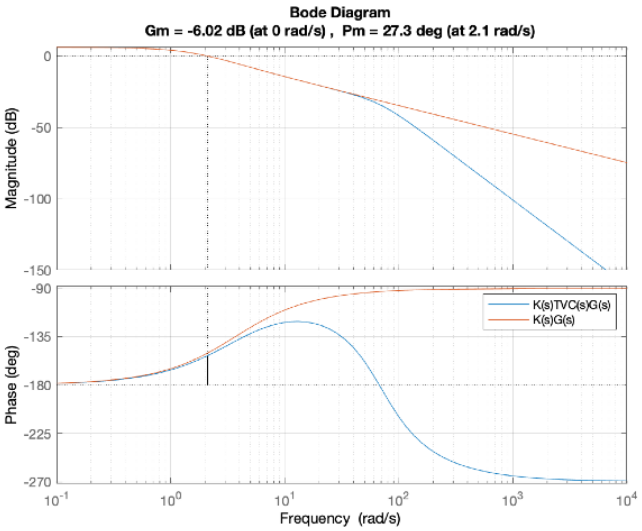

Figure 10: Bode diagram of the controlled system with TVC actuator dynamics

The TVC actuator dynamics is also represented as a Nichols plots in Fig. 11. Including TVC dynamics, a rigid GM appears at 33.9 deg.

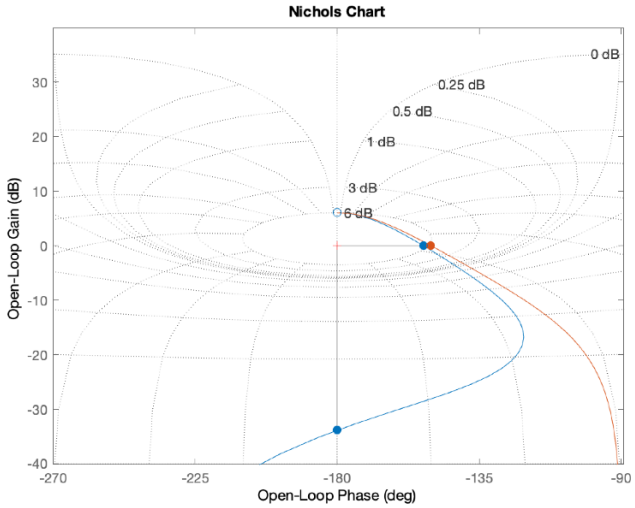

Figure 11: Nichols plots of open-loop controlled system $K(s)G(s)$ without (blue line) and with TVC controlled dynamics $K(s)TVC(s)G(s)$ (orange line)

3.4 Drift control

Considering drift, performance requirements must be fulfilled. These are reported in Table 3.

The appearance of aerodynamic load is mainly due to wind disturbances. It can be expressed as

$$Q_\alpha = Q(\theta + \frac{\dot{z}}{V} - \alpha_\omega) \tag{36}$$

So, minimizing the angle of attack (Eq. 3) , the aerodynamic load can be decreased. To minimize the α variations, a θ feedback controller can be used [13]. Since the fundamental time constant of the lateral drift dynamics is much greater than that associated to the attitude dynamics, an appropriate selection of K_θ may be obtained by analyzing the so called quasi steady-state form of the rigid body equation [14]. Here we will set to zero the first and high order derivatives in θ.

From the equation of rigid-body attitude dynamics (Eq. 1), we may obtain

$$\ddot{\theta} = A_6\alpha + K_1\beta \tag{37}$$

Using the calculated PD, β control can be defined:

$$\beta(s) = -(K_{P_\theta} + K_{D_\theta}s)\theta(s) \tag{38}$$

The transfer function results in

$$\theta(s) = \frac{A_6}{s^2 + K_1 K_{D_\theta} s + (K_1 K_{P_\theta} - A_6)} (\frac{\dot{z}_{ss}}{V} - \alpha_\omega) \tag{39}$$

where $\dot{z}_{ss}$ is the drift rate value at steady-state. Setting the derivatives of θ to zero we can find θ at steady-state

$$\theta_{ss} = \frac{A_6}{(K_1 K_{P_\theta} - A_6)} (\frac{\dot{z}_{ss}}{V} - \alpha_\omega) \tag{40}$$

Finally, knowing the relation between angles, we may calculate α at steady-state

$$\alpha_{ss} = \frac{K_1 K_{P_\theta}}{(K_1 K_{P_\theta} - A_6)} (\frac{\dot{z}_{ss}}{V} - \alpha_\omega) \tag{41}$$

The minimum angle of attack will be achieved for $K_{P_\theta} = 0$. However, this condition makes the system unstable. In this way, to limit the aerodynamic load and the lateral drift, additional feedback on drift z and drift rate $\dot{z}$ is introduced, so as to obtain the controller

$$K_{BC}(s) = \begin{bmatrix} K_{P_\theta} & K_{D_\theta} & K_{P_z} & K_{D_z} \end{bmatrix} \tag{42}$$

With regard to the θ proportional control, even though it has an effect on α, it is difficult to select a value of K_{P_θ} which both satisfies stability requirements and performance in terms of angle of attack or aerodynamic load.

On the other hand, small values for K_{P_θ} and K_{D_θ} may reduce lateral drift and aerodynamic loads without jeopardizing the attitude tracking performance. However, using large values of K_{P_θ} and K_{D_θ} the system will become unstable.

The definition of the elements of K_{BC}, will be discussed in the following section.

4 Controller design

In this section and based on the theory explained in Section 3, the parameters that will compose the PD controller are designated. This will be done with two different procedures based on pole placement methodology in order to study the most efficient, regarding stability, performance and robustness.

As already mentioned, the two main objectives will be to obtain minimum drift and load minimum always inside the requirements established in Subsection 3.1.

4.1 System architecture

First of all, it must be understood the architecture chosen to model the LV system. Figure 12 shows the composition used in Simulink software in order to simulate the system.

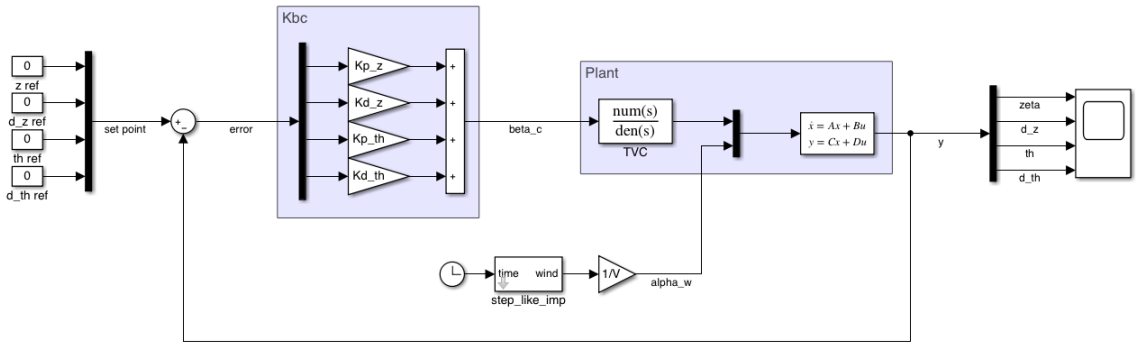

Figure 12: System architecture scheme

The plant is represented by the space state form of the EoM (Eq. 16), multiplied to the TVC transfer function (Eq. 21). Moreover, there is a feedback channel for each element of the state vector and multiplied by the gain matrix $\mathbf{K_{BC}}$ (Eq. 42). The reference term is scaled to ensure there is no steady-state reference tracking error, which in this case all states are set to zero.

Thus, there are two inputs going through the plant, β_c is the controlled input found after the PD controller and α_ω is disturbance simulated in this case by the synthetic step-like wind gusts defined in Subsection 2.3, divided by the forward velocity V of the LV. The system is frozen at $t = 72$ s (Table 1) being this the point of highest dynamic pressure condition and for that, the most critical one.

4.2 Pole placement

In feedback control system theory, pole placement, also known as Full State Feedback (FSF), is a technique used to position a plant closed-loop poles at predetermined places.

The primary function of state feedback control is to stabilize a system so that all of its closed-loop eigenvalues are located in the left side of the complex plane. Pole placement provides a prerequisite for placing system poles in the desired positions. [15]

Considering a plant with input $\mathbf{u}$ (Eq. 13) and output $\mathbf{y}$ (Eq. 17), the goal is to develop a feedback control system that drives the output to some desired value. This can be done by comparing the output to a reference signal to get the control error and develop a controller

that uses that error to generate the input signals into the plant with the mission of driving the error to zero. [5]

Using the pole placement method, this problem may be approached by, rather than feedback of the output y, feedback of the value of each state variable in the state vector (Eq. 18). The state vector is then multiplied by a matrix that is made up of a collection of different gain values (Eq. 42), the result is subtracted from a scaled reference signal and this result is fed directly into the plant as the input, as seen in Fig. 12. Pole placement is a method by which the proper gain matrix can be calculated to guarantee system stability. [16]

With respect to the plant, the $\mathbf{A}$ matrix captures the dynamics of the system. Any feedback controller has to modify the $\mathbf{A}$ matrix in order to change the dynamics of the system. The eigenvalues of the matrix are the poles of the system and the location of the poles dictates stability of a linear system. [15]

That is the key to pole placement, generating the required closed-loop stability by moving the poles or the eigenvalues of the closed-loop $\mathbf{A}$ matrix.

In a mathematical view [5], the structure defined varies the inputs value as:

$$\mathbf{u} = \mathbf{r} - \mathbf{K}\mathbf{x} \tag{43}$$

Plugging this control input into the state equation, the loop is being closed and the following state equation is obtained:

$$\dot{\mathbf{x}} = \mathbf{A}\mathbf{x} + \mathbf{B}(\mathbf{r} - \mathbf{K}\mathbf{x}) \tag{44}$$

or

$$\dot{\mathbf{x}} = (\mathbf{A} - \mathbf{B}\mathbf{K})\mathbf{x} + \mathbf{B}\mathbf{r} \tag{45}$$

$(\mathbf{A} - \mathbf{B}\mathbf{K})$ is the closed loop $\mathbf{A}$ matrix and the ability to move the eigenvalues is then achieved by choosing an appropriate $\mathbf{K}$. This will be proceeded in the following subsections.

4.3 Manual Pole Placement

At first, the design of the new $\mathbf{K_{BC}}$ controller will be done through a manual pole placement method. To this end, the ability to place closed-loop poles wherever is chosen is achieved, assuming the system is controllable and observable.

The rigid body system is initially unstable (Fig. 6) so the incorporation of $\mathbf{K_{BC}}$ is compulsory. As a first attempt it will be studied the effect of K_{P_θ} and K_{D_θ} already calculated (Eqs. 29 and 35).

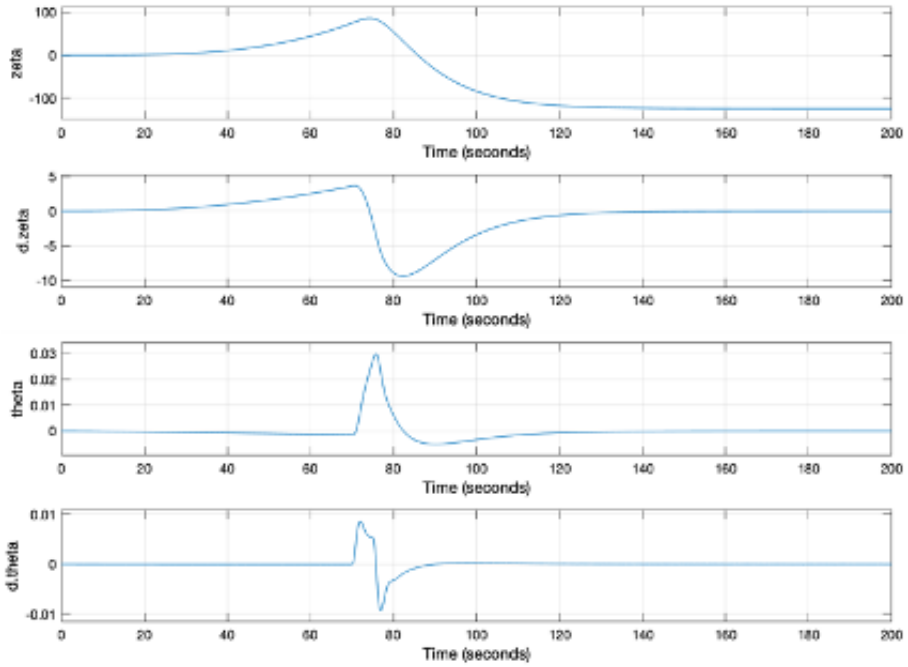

Figure 13: Model wind 1 input response to PD pitch controller

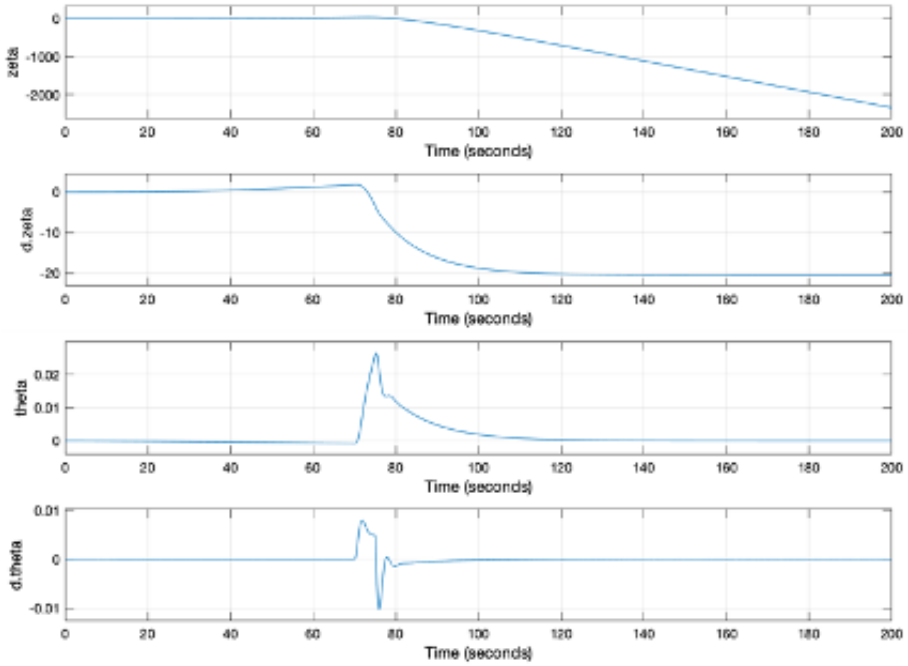

Figure 14: Model wind 2 input response to PD pitch controller

In both cases (Figs. 13 and 14), pitch stability has been achieved as $\dot{\theta}$ reaches the steady condition after the disturbance has stabilized. However, for the wind model 2 (Fig. 14), drift is still unstable, illustrated with the divergence of z. In this degree, the implementation of a PD controller regarding drift is also needed. As previously stated, this controller must have small values to guarantee stability.

The best results found with this method have been for

$$K_{P_z} = -0.0008; \qquad K_{D_z} = -0.005; \qquad K_{P_\theta} = 1.8; \qquad K_{D_\theta} = 1.5; \tag{46}$$

To find this values it has been followed a manual process described in Annex A.1.

The final results are plotted in Figs. 15 and 16.

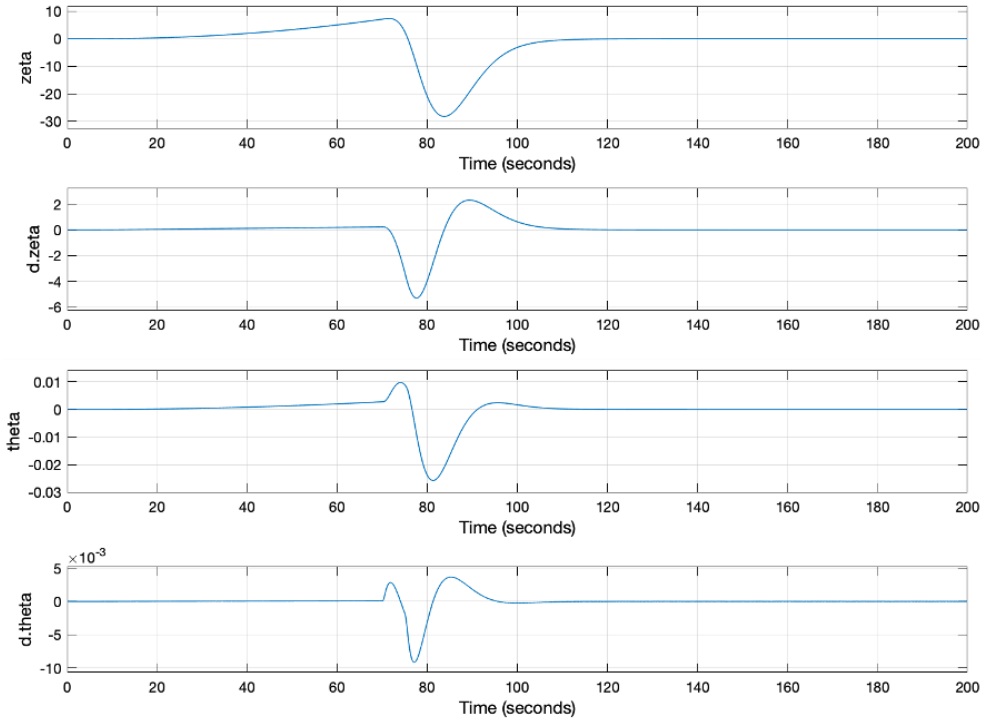

Figure 15: Model wind 1 input response to final PD controller

Fig. 15 shows how, after the action of a wind disturbance (model wind 1), both drift and pitch angle return to the reference position. However, in Fig. 16, a small error appears in the performance of z and θ after dealing with the model wind 2 input, although inside the defined margins (Table 3).

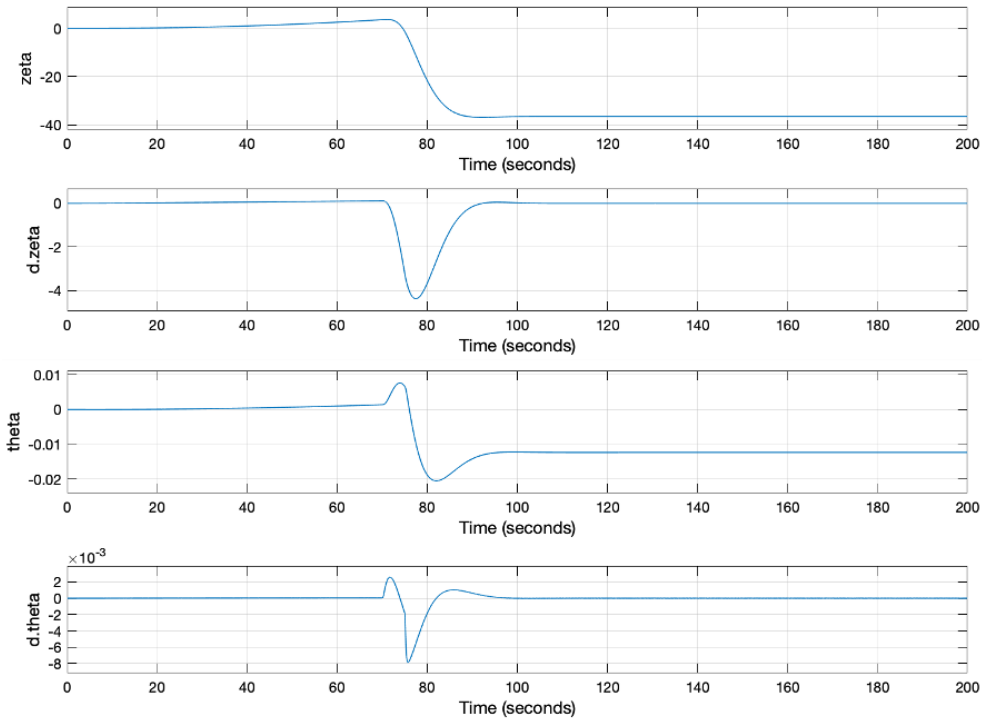

Figure 16: Model wind 2 input response to final PD controller

In order to see if the final results meet the requirements, the response of the TVC angle and the aerodynamic load are obtained. For both input wind gusts, the results of the controlled TVC angle β_c obtained are illustrated in Figs 17 and 18.

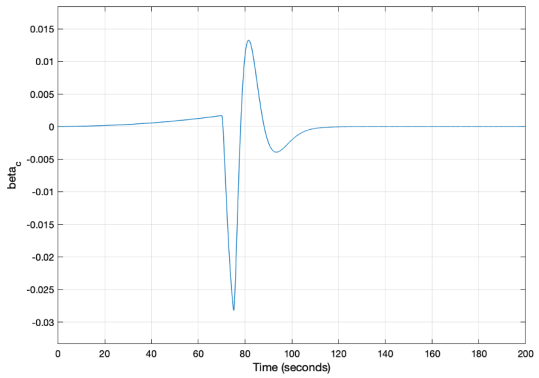

Figure 17: β_c response to model wind 1 input

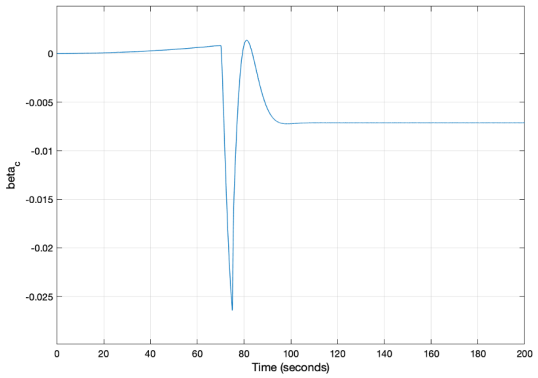

Figure 18: β_c response to model wind 2 input

Fig. 17 shows how, once the wind disturbance returns to a steady condition, β_c goes to zero. While in Fig. 18, where the wind disturbance is not zero at equilibrium, there is a need of a small TVC angle in order to follow the reference trajectory. This is in relation with the fact that $\dot{z}$, θ and β are all proportional to each other (Eqs. 1 and 2), and being $\dot{z}$ and θ different from zero (Fig. 16), β_c could not possibly be zero at stability.

The aerodynamic load is calculated considering that, at the frozen time considered ($t = 72$ s), the LV is at an altitude of $h = 15143$ m and has a forward velocity of $V = 937.70$ m/s (Table 1). For that reason we can obtain the dynamic pressure as

$$Q = \frac{1}{2}\rho(h)V^2; \qquad \rho(h) = 0.15595\rho_0 \tag{47}$$

And from Eq. 36 we have:

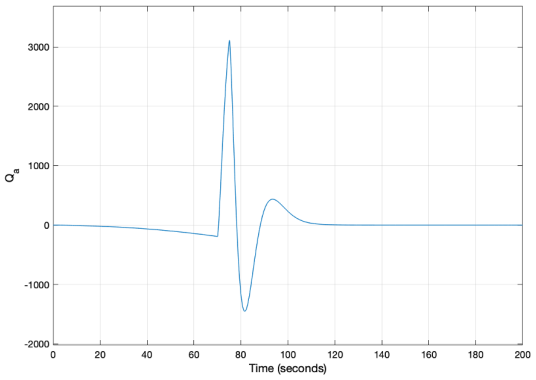

Figure 19: $Q\alpha$ response to model wind 1 input

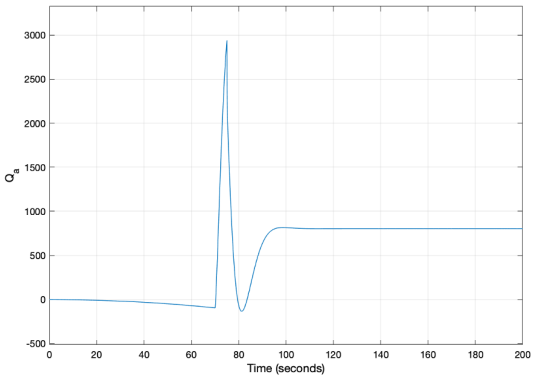

Figure 20: $Q\alpha$ response to model wind 2 input

The aerodynamic load has linear relation with the sum of $\frac{\dot{z}}{V}$, θ and α_ω (Eq. 36). In this way, for model wind 1 input, having all these parameters reaching the steady condition, Q_α is also close to zero at equilibrium (Fig. 19). Whereas in Fig. 20, the aerodynamic load is different from zero as the wind disturbance is not null and neither are the drift rate and pitch angle obtained. For this reason, the mission of obtaining small values of $\dot{z}$ and θ is determined to reaching minimum load in the LV.

To have a clearer view, the obtained results are presented in Table 4.

Parameters	**Wind Model 1**	**Wind Model 2**
Aerodynamic load	$\simeq 0$ N	803.1 N
Lateral drift	$\simeq 0$ m	-36.56 m
Lateral rate drift	$\simeq 0$ m/s	$\simeq 0$ m/s
TVC angle deflection	$\simeq 0$ deg	-0.4072 deg

Table 4: Performance parameters for final PD controller

These are inside the performance requirements defined in Table 3.

Regarding stability margins, the controller proposed, together with the system, develops an Aero Gain Margin of 6.44 dB, a Rigid Phase Margin of 71.6 deg and a Rigid Gain Margin of 23 dB as represented in Fig. 21, which considering Table 2, is inside the margins established.

The improvement with respect to the system which only used pitch control (Eq. 35) can be analysed through Fig. 21.

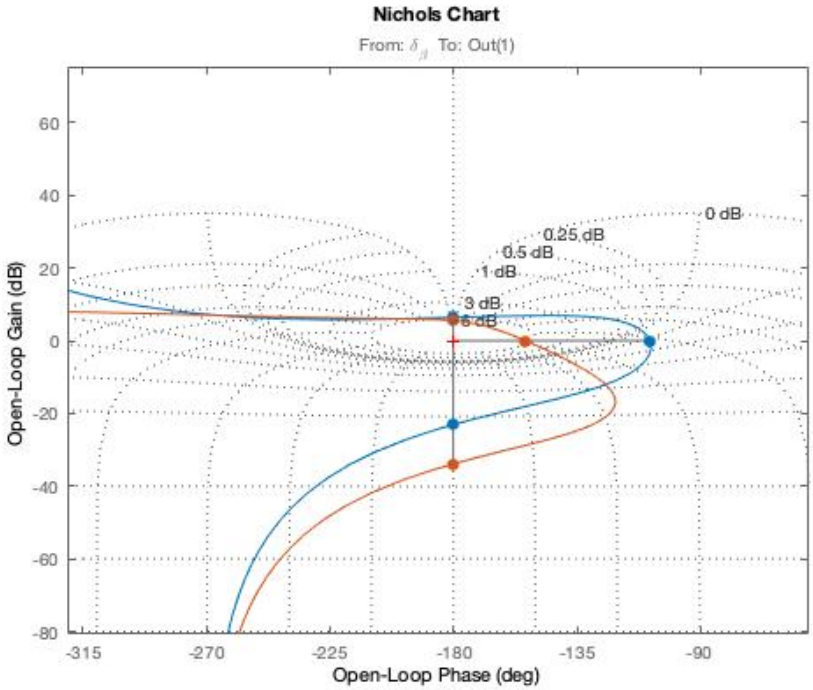

Figure 21: Nichols plots of open-loop controlled system $K(s)TVC(s)G(s)$ (orange line) and $K_{BC}(s)TVC(s)G(s)$ (blue line)

Both Aero GM and Rigid PM are improved as the curve translates upwards and to the right, although with a cost of lower Rigid GM, which is still inside the requirements.

4.4 Linear Quadratic Regulator

The controller will also be designed by a different method. A Linear Quadratic Regulator is a type of optimal control that is based on state-space representation.

Being this also a type pole placement, LQR controllers also feed back the full state vector, multiplying it by a gain matrix **K** and subtracting it from the scaled reference. So the structure of these two control laws is the same (Fig. 12). However, how **K** is chosen is different.

In LQR pole locations are not picked, but the optimal **K** matrix is found by choosing closed-loop characteristics that are important to the mission. Specifically, how well the system performs and how much effort does it take to get that performance.

In short, LQR computes control signals by simulating the situation as an optimization problem. In other words, it attempts to provide control signals that minimize a cost function. [17]

Considering a linear time-invariant system in state-space form as Eq. 16, the cost function will be given by a quadratic cost function which quantifies the performance of the controller

$$J = \int_0^\infty [\mathbf{x}^T\mathbf{Q}\mathbf{x} + \mathbf{u}^T\mathbf{R}\mathbf{u}]dt, \qquad \mathbf{Q} = \mathbf{Q}^T \leq 0, \quad \mathbf{R} = \mathbf{R}^T > 0 \tag{48}$$

Q is a square matrix NxN (N=number of states) and defines the performance whilst **R** defines the effort.

Since the only controlled variable in this case is the TVC angle β, the specific cost function to minimize is expressed as

$$\min \beta_c \int_0^\infty (\mathbf{x}^T\mathbf{Q}\mathbf{x} + \beta_c^2)dt \tag{49}$$

Q is a user defined matrix that tells the solver which combination of states to minimize. And the input thrust angle is also trying to be minimized by **R**. At first these two matrices will be defined as

$$\mathbf{Q} = \begin{bmatrix} 1 & 0 & 0 & 0 \\ 0 & 1 & 0 & 0 \\ 0 & 0 & 1 & 0 \\ 0 & 0 & 0 & 1 \end{bmatrix}; \quad \mathbf{R} = 1; \tag{50}$$

The mathematics of this process are very time consuming and complex. In order to simplify the process, the calculus is done in Matlab software with the function ***K=lqr(A,B,Q,R)***, where **Q** and **R** are the previously defined matrices and **A** and **B** are the matrices corresponding to the state space representation of the system. Obtaining the matrix **K**, it can now be substituted in the gains of the system.

Thus, it is first analyzed the performance and stability for this case.

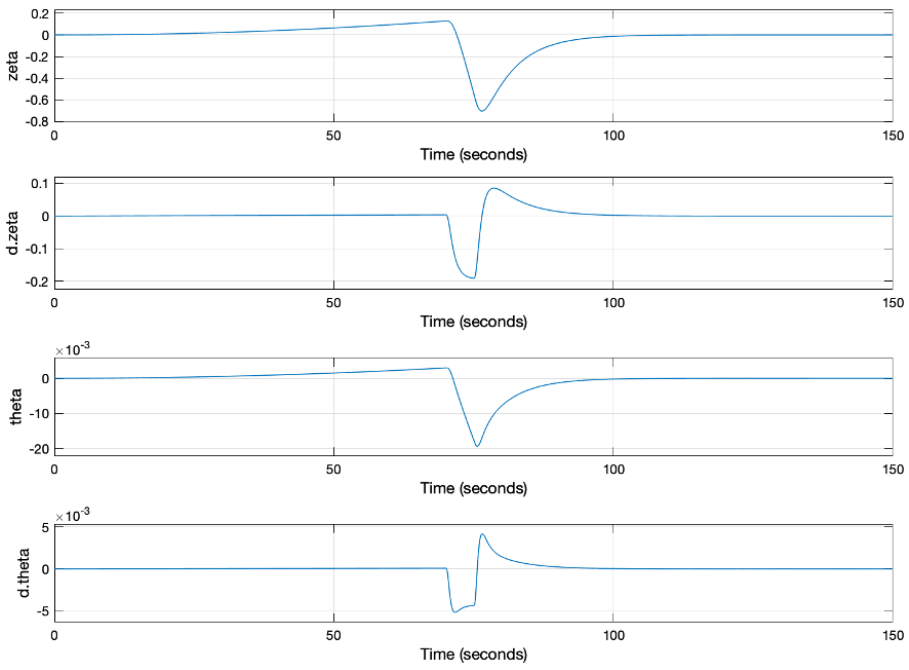

Figure 22: Response to model wind 1 input with LQR controller

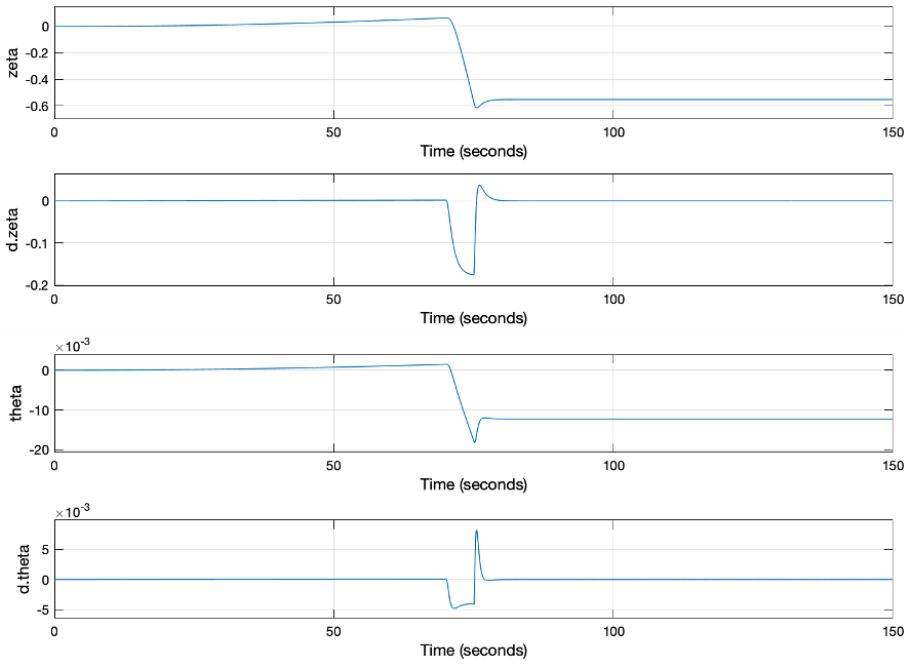

Figure 23: Response to model wind 2 input with LQR controller

The plots obtained (Figs. 22 and 23) show all parameters are within the margins for both wind model inputs. Similarly, to the controller designed in Subsection 4.3, for the response to model wind 2 input (Fig. 23), drift rate and pitch angle present small errors with respect to the reference point.

In the case of stability, Fig. 24 illustrates how the system now has an Aero GM of 18.9 dB, a Rigid PM of 42.9 deg and a Rigid GM of 9.57 dB.

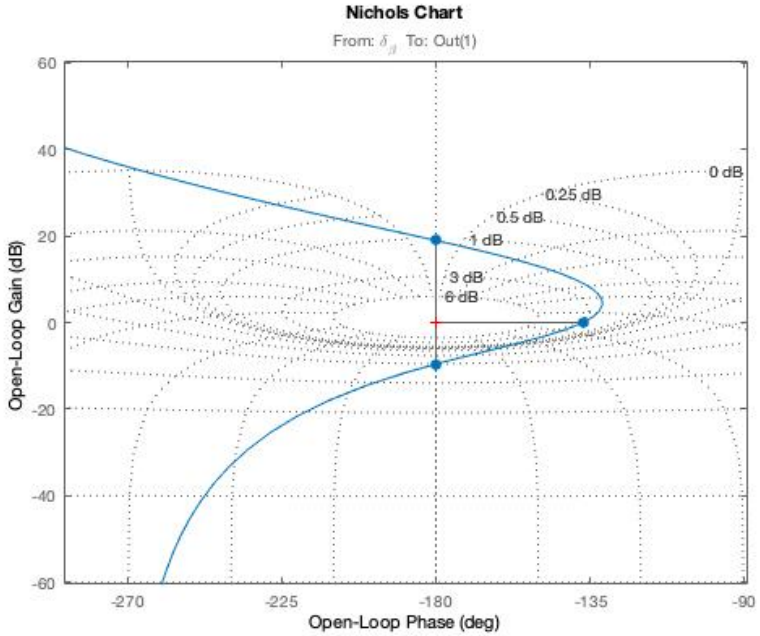

Figure 24: Nichols plot for initial LQR controller

Having stability margins inside the desired range, the mission is to improve the signal shape of Figs. 22 and 23 paying attention to time response and overshoot.

The difficulty of this method is that although it is indeed more intuitive the choice of parameters to vary, in every variation of **Q** and **R** to improve any performance aspect, it must be checked that the stability of the system has not been jeopardized.

After some tryouts, the best results have been obtained by **Q** and **R** matrices defined as follows. The process of design is developed in Annex A.2.

$$\mathbf{Q} = \begin{bmatrix} 5 & 0 & 0 & 0 \\ 0 & 0.01 & 0 & 0 \\ 0 & 0 & 1 & 0 \\ 0 & 0 & 0 & 1 \end{bmatrix}; \quad \mathbf{R} = 0.1; \tag{51}$$

The calculated gains that compose matrix **K** are

$$K_{P_z} = -7.0711; \qquad K_{D_z} = -5.0763; \qquad K_{P_\theta} = 98.2365; \qquad K_{D_\theta} = 29.3690; \tag{52}$$

Fig. 25, shows the stability margins obtained by incorporating the new **K** matrix into the system. These will be Aero GM at 14 dB, Rigid PM at 34.2 deg and Rigid GM at 8.52 dB.

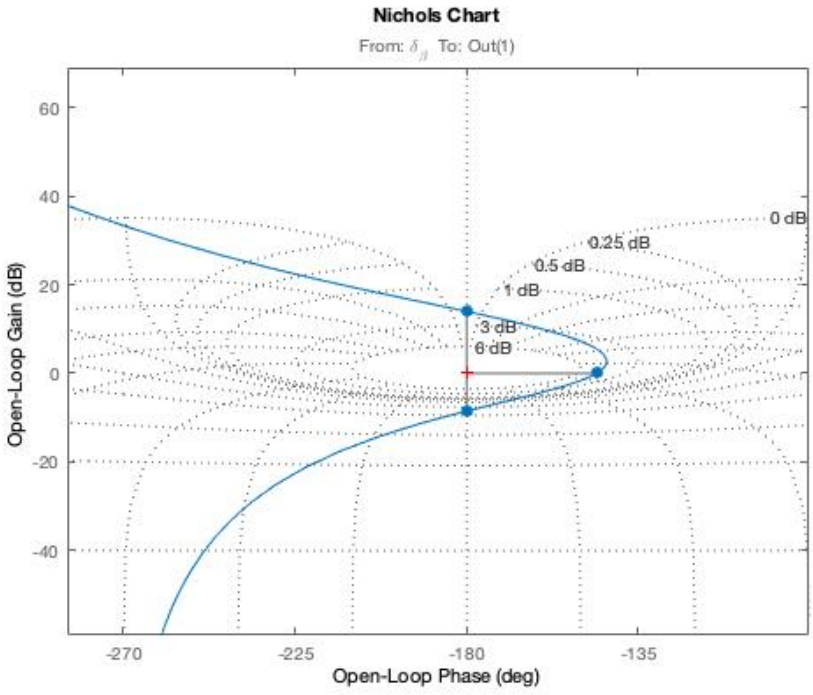

Figure 25: Nichols plot for final LQR controller

Now, with regard to performance, it is going to be studied the equilibrium reached for each parameter.

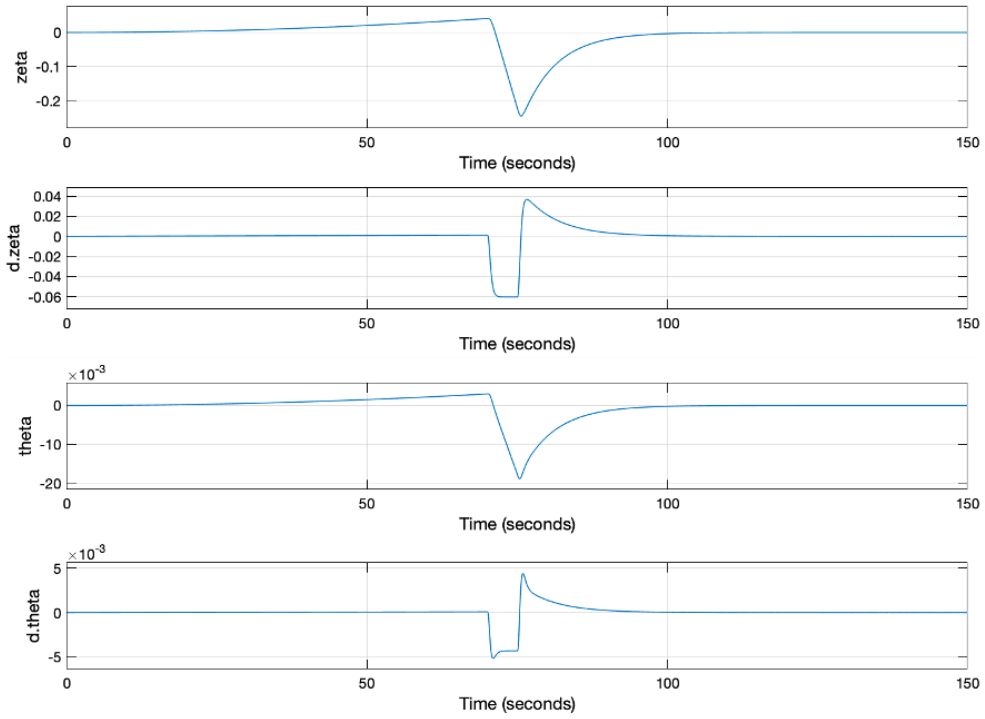

Figure 26: Response to model wind 1 input with final LQR controller

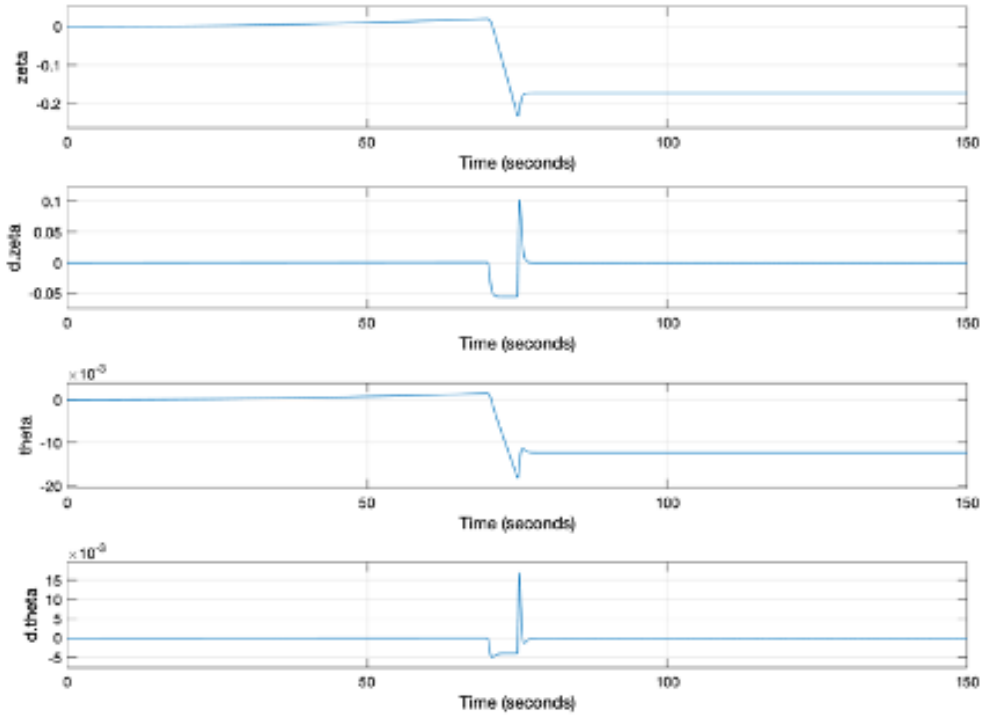

Figure 27: Response to model wind 2 input with final LQR controller

Figs. 26 and 27 display there has been an improvement in minimizing the error of drift with respect to the previous results (Figs. 22 and 23), specifically in the response to model wind 2 input. The deviation of drift has been lowered by almost 0.4 m and with a better

time response.

From the error minimization, it is also minimized the cost of β and the aerodynamic load. Figs. 28 and 29 show the TVC angle needed in the equilibrium is very small.

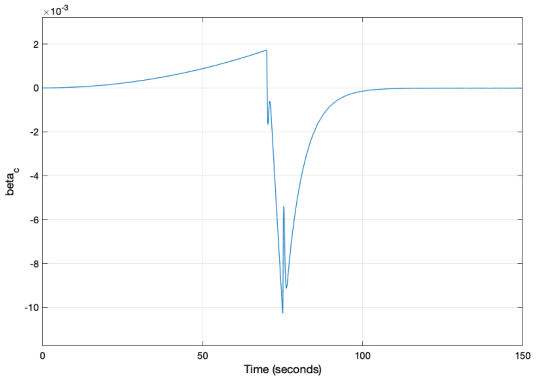

Figure 28: β_c response to model wind 1 input for final LQR controller

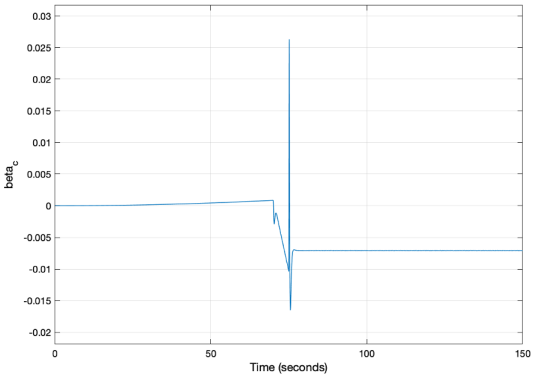

Figure 29: β_c response to model wind 2 input for final LQR controller

Likewise, the aerodynamic load experienced for both wind inputs is plotted in Figs. 30 and 31. As in previous cases, aerodynamic load is only present after the system has confronted to wind model 2 input (Fig. 31).

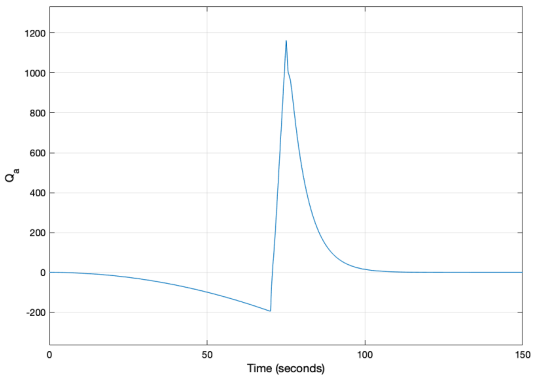

Figure 30: $Q\alpha$ response to model wind 1 input for final LQR controller

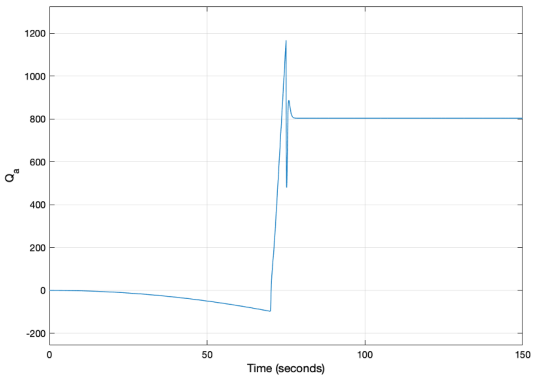

Figure 31: $Q\alpha$ response to model wind 2 input for final LQR controller

Table 5 illustrates all the steady state responses seized during this process.

Parameters	**Wind Model 1**	**Wind Model 2**
Aerodynamic load	-0.002199 N	803.1 N
Lateral drift	$\simeq 0$ m	-0.1719 m
Lateral rate drift	$\simeq 0$ m/s	$\simeq 0$ m/s
TVC angle deflection	$\simeq 0$ deg	-0.4071 deg

Table 5: Performance parameters for final LQR controller

As mentioned, these are also inside the performance requirements defined in Table 3.

5 Results and discussion of the differences among the considered methods

Aiming to analyze the diversity between the two traditional methods, the response of both designs previously described is compared.

First, the difference in the steady state reached is analysed. Tables 4 and 5 are recalled in Table 6.

	POLE PLACEMENT		LQR	
Parameters	**Wind M1**	**Wind M2**	**Wind M1**	**Wind M2**
Aerodynamic load	$\simeq$ 0 N	803.1 N	-0.002199 N	803.1 N
Lateral drift	$\simeq$ 0 m	-36.56 m	$\simeq$ 0 m	-0.1719 m
Lateral rate drift	$\simeq$ 0 m/s	$\simeq$ 0 m/s	$\simeq$ 0 m/s	$\simeq$ 0 m/s
TVC angle deflection	$\simeq$ 0 deg	-0.4072 deg	$\simeq$ 0 deg	-0.4071 deg

Table 6: Performance comparison for final controllers

From Table 6 it is understood that, for the first wind model input, all parameters reach a value close to the reference position. This is due to the fact that the step input (Fig. 3) starts and finishes in the resting condition. For the second step input (Fig. 4), the nozzle angle is different from zero. This steady state error is due to the fact that model wind input 2 does not return to the resting position but keeps maintaining velocity. Therefore, it is required to deflect the TVC angle to compensate for this disturbance. Comparing both designs, there is a lower trajectory error in the LQR method although the objectives of load minimum and smaller effort with respect to TVC angle are almost the same in both controllers. Whether the difference in drift achieved is significant enough will be discussed after studying other characteristics of the response.

In the next step, the shape of the response signals is evaluated. Figs. 32, 33, 34, 35 plot the signals obtained from both controllers. Plots in orange correspond to the manual pole placement and blue plots, to the LQR.

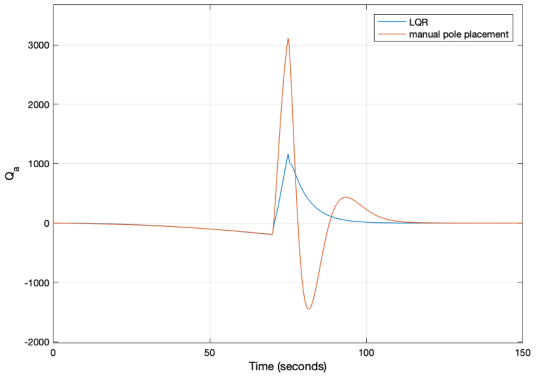

Figure 32: Comparison $Q\alpha$ response to model wind 1 input for both controllers

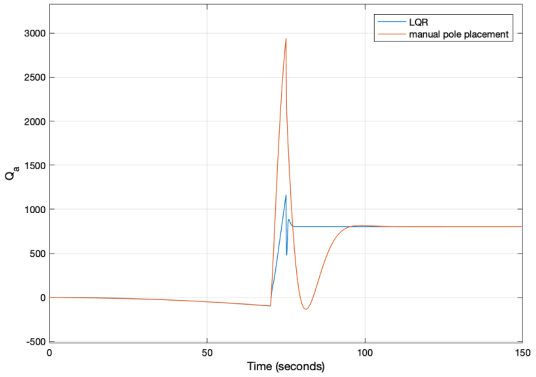

Figure 33: Comparison $Q\alpha$ response to model wind 2 input for both controllers

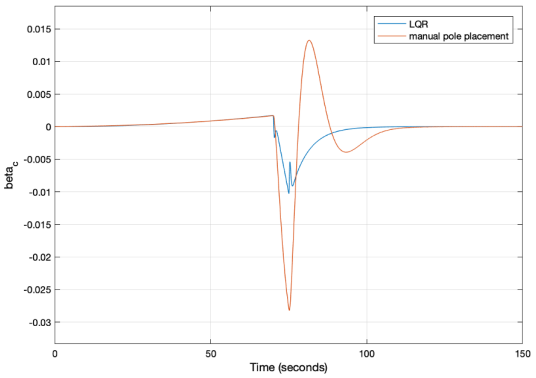

Figure 34: Comparison β_c response to model wind 1 input for both controllers

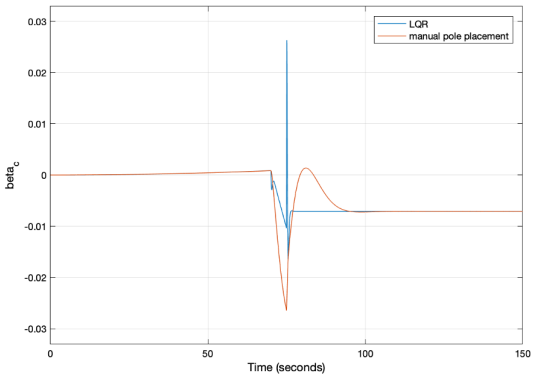

Figure 35: Comparison β_c response to model wind 2 input for both controllers

As described before, Figs. 32, 33, 34, 35 illustrate how the aerodynamic load and TVC angle deflection are almost the same in both controllers when equilibrium has been reached. Moreover, in all cases, the transition to the final response is more aggressive in the LQR controller while it has a smaller time response.

Fig. 36 reports the response of both controllers with model wind 1 as input. All parameters end in a steady condition. With the LQR controller, drift is close to be constant and pitch experiences a small overshoot before returning to the reference position. While with the manual pole placement controller, both pitch and drift take more time to find the steady condition with bigger trajectory error during the path.

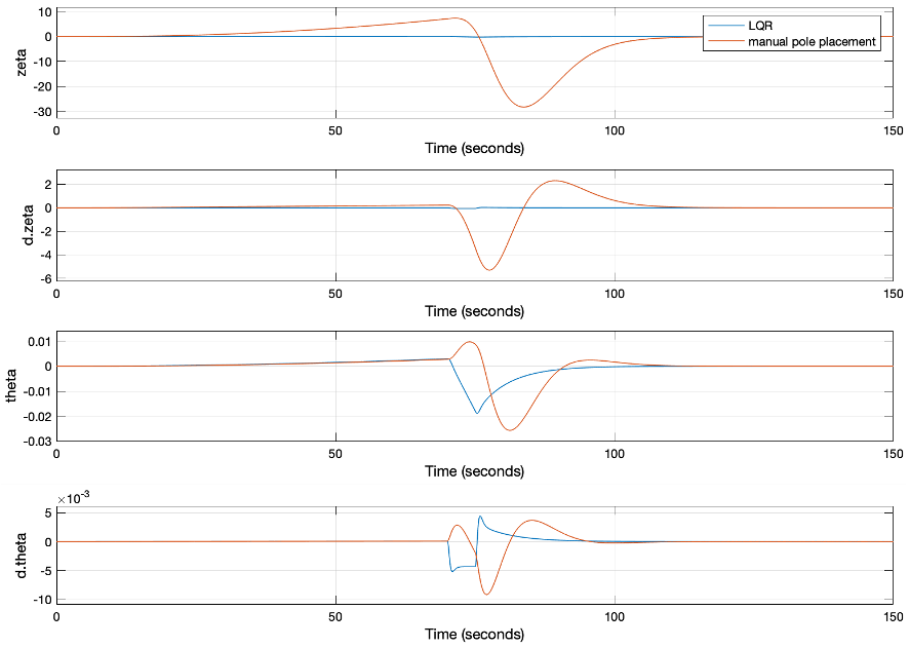

Figure 36: Comparison response to model wind 1 input for both controllers

Fig. 37 shows the response of both controllers with model wind 2 as input. Both pitch and drift experience a small error in the trajectory once equilibrium has been reached. The main difference between both is the improvement on drift performance obtained with the LQR controller. LQR controller also reaches equilibrium quicker although with a more aggressive transition. Moreover, it is important to highlight how the first PD controller (manual pole placement) experiences a higher overshoot.

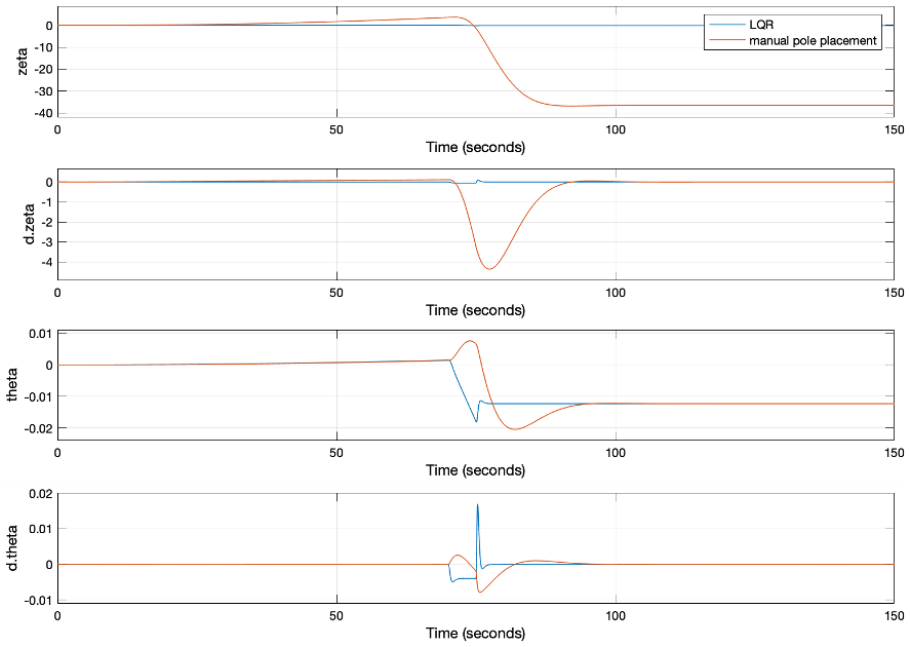

Figure 37: Comparison response to model wind 2 input for both controllers

Finally with regard to stability, Fig. 38 presents the Nichols plots drawn by each controller.

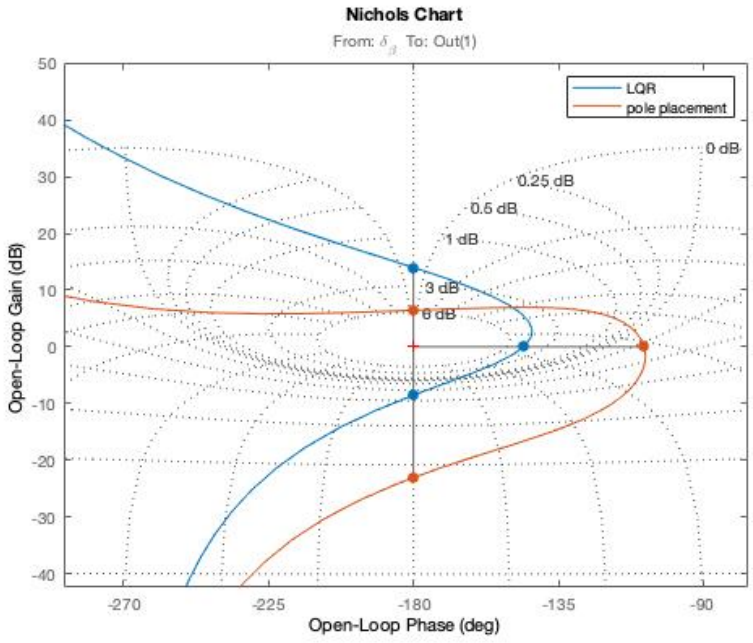

Figure 38: Nichols plots of pole placement controlled system (orange line) and LQR controlled system (blue line)

It is apparent that the Aero GM is increased with the LQR controller at a cost of reducing the Rigid PM and Rigid GM. Both controllers fulfil stability requirements as already stated.

6 Conclusions

In conclusion, both methods cover the need of guarantying stability and performance inside the determined restrictions. The selection of the best controller will depend on whether it is more critical to obtain a quicker response or having a smother transition will depend on the mission of each project.

On the other hand, with respect to the optimization process, the design of the LQR controller has turned out to be less time consuming and more intuitive. The fact that its design is based on giving importance to certain characteristics, makes the parameters that are modified each time more intuitive.

6.1 Accomplishments

During the work, it has been possible to fulfill the principal objectives mentioned at the beginning of the report.

The design of a Flight Control System has been developed in two different ways, attending to the need of ensuring a favorable stability of the system and the correct performance of the model. The control system is a classical gain-scheduled proportional-derivative (PD) controller, to stabilize rigid-body dynamics.

It has been taken into account how a proper trajectory performance of drift rate and pitch angle will guarantee minimum load. Moreover, it is appreciated that stability and performance have an inversely proportional relation in such that the improvement of one may jeopardize the other's outcome. The classical 'drift-minimum' and 'load-minimum' control principles have been pursued, as well as the robustness with respect to possible loss of performance due to model uncertainties, off-nominal flight conditions, and unexpected wind gust disturbances.

The most difficult task is to find control system parameters that satisfy both the stability and robustness requirements as well as performance in terms of error tracking and disturbance rejection. As a result, an iterative and time-consuming procedure is required to reach a good compromise between competing flight control system requirements.

Finally, having worked with the two different methods, the efficiency of traditional control theory in such complicated systems has been studied and the importance of the implementation of new techniques in the current days has been understood.

6.2 Future work

Regarding an improvement on the work in the future, it would be interesting to consider the design of a bending filter. Having already developed a rigid body controller, the inclusion of a bending filter would also take into account the flexible dynamics of the system.

However, it should be considered that the incorporation of this new element could jeopardize the effectiveness of the controller already designed. There is a need to re-tune the controller in a iterative process until the desired results are reached.

References

[1] Curtis R. Amble. "Thrust Vector Control of an Overexpanded Supersonic Nozzle using Pin Insertion and Rotantino Airfoils". In: (1991).

[2] T. Benson. *Rocket Stability.* 2021. URL: https://www.grc.nasa.gov/www/k-12/rocket/rktstab.html.

[3] Hidehiko Mori. "Control system design of flexible-body launch vehicles". In: (1999).

[4] H Charles. "Ares I Flight Control System Overview". In: *AIAA Guidance, Navigation and Control Conference* (2008).

[5] Róbert Szabolcsi. "Pole Placement technique applied in Unmanned Aerial Vehicles automatic Flight Control Systems Design". In: *Land Forces Academy Review* (2018).

[6] A. L. Greensite. "Analysis and design of space vehicle control systems - short period dynamics of attitude control during launch and autopilot design". In: *NASA Technical report NASA-CR-826, GD/C-DDE66-028* (1967).

[7] D.Garner. "Control Theory Handbook". In: *NASA Technical report NASA- TM-X-53036, NASA Marshall Space Flight Center* (1964).

[8] Choong-Seok Oh and Hyochoong Bang. "Attitude Control of Flexible Launch Vehicle using Adaptive Notch Filter". In: *Korea Advanced Institute of Science and Technology* (2005).

[9] J. H. Jung. "Modeling, and classical and advanced control of a solid rocket motor thrust vector control system". In: *Master Thesis MIT* (1993).

[10] A. L. Greensite. "Analysis and design of space vehicle flight control systems. volume i-short period dynamics". In: *NASA-CR-820, GD/C-DDE65-055* (1967).

[11] Domenico Trotta. "Adaptive control of launch vehicles in atmospheric flight [Tesi di dottorato]". In: (2021).

[12] A. Marcos P. Simplício S. Bennani and C. Roux. "Structured singular-value analysis of the vega launcher in atmospheric flight". In: *Journal of Guidance, Control, and Dynamics, pp. 1342–1355* (2016).

[13] R. F. Hoelker. "Theory of artificial stabilization of missiles and space vehicles with exposition of four control principles". In: *NASA Technical Note, NASA TN D-555* (1961).

[14] A. L. Greensite. "Analysis and design of space vehicle flight control systems. volume vii-attitude control during launch". In: *NASA-CR-826, GD/C- DDE66-028* (1967).

[15] J.Åström B.WittenmarkK. *Some Aspects on Pole-placement Design.* 2017. URL: https://www.sciencedirect.com/science/article/pii/S1474667017520972.

[16] Jitendra R. Raol and Ramakalyan Ayyagari. *Pole Placement Design Technique.* 2019. URL: https://www.ece.rutgers.edu/~gajic/psfiles/poleplacement.pdf.

[17] Nikolai Matni Yuh-Shyang Wang and John C. Doyle. "Localized LQR Optimal Control". In: *arXiv:1409.6404 [cs, math]* (2014).

Annexes

A Gain search

A.1 Manual pole placement gain search

The design of the first controller follows a manual process. The responses are obtained from the simulation of the system (Fig. 12) in MATLAB Simulink. All tests are done with the wind model 2 (Fig. 4) as input, which is a more critical condition. Using the wind model 1 (Fig. 3), only performance results will be modified although with a better outcome, stability is independent of the input used.

The below table collects the different tests performed in the search for the better controller $\mathbf{K_{BC}}$ design. In all cases, stability of the system and performance of maximum drift and TVC angle deflection are studied.

K_{P_z}	K_{D_z}	K_{P_θ}	K_{D_θ}	z_{max}	β	Aero GM	Rigid PM	Rigid GM
0	0	1,4866	0,4037	-2340	0	5,56	26,4	33,9
-0,001	0	1,4866	0,4037	-26,4	-0,3461	3,86	-10,5	33,9
-0,0001	0	1,4866	0,4037	-255	-0,401	5,42	26,4	33,9
-0,00001	0	1,4866	0,4037	-1618	-0,1825	5,55	26,4	33,9
-0,0001	**-0,01**	1,4866	0,4037	-171,4	-0,3871	2,37	12,1	34,8
-0,0001	**-0,001**	1,4866	0,4037	-253,9	-0,402	5,14	25,1	34
-0,0001	**-0,0001**	1,4866	0,4037	-254,4	-0,4025	5,4	26,3	33,9
-0,0001	-0,0001	**1,7**	0,4037	-279,5	-0,3973	6,51	25,5	33,8
-0,0001	-0,0001	**1,3**	0,4037	-231,1	-0,4076	4,27	26,6	34
-0,0001	-0,0001	1,7	**0,7**	-279,7	-0,3963	6,75	46,8	29,3
-0,0001	-0,0001	1,7	**0,9**	-279,7	-0,3956	6,81	58,3	27,2

In order to understand better the results, it is arranged a color pattern, where green expresses that the requirements have been fulfilled; yellow, that they are close to be met; and red, that they are far from the desired value. Moreover, in bold, the controller elements that are being varied are highlighted.

Starting (first row) from the baseline controller (Eq. 25), drift and pitch gains are modified individually to evaluate the effect on the result. Using the BC, drift performance is outside the requirements although there is no need to deflect the TVC angle. Regarding stability, the required margins are almost reached. Including a small drift proportional gain K_{P_z}, stability margins are heavily jeopardized although drift performance is improved. For a low magnitude K_{D_z} stability can be improved considerably. Lastly, both K_{P_θ} and K_{D_θ} are increased a bit to obtain the desired stability margins, always checking the performance is desirable.

Once all values are inside the requirements of Tables 2 and 3, it is analysed the response signal.

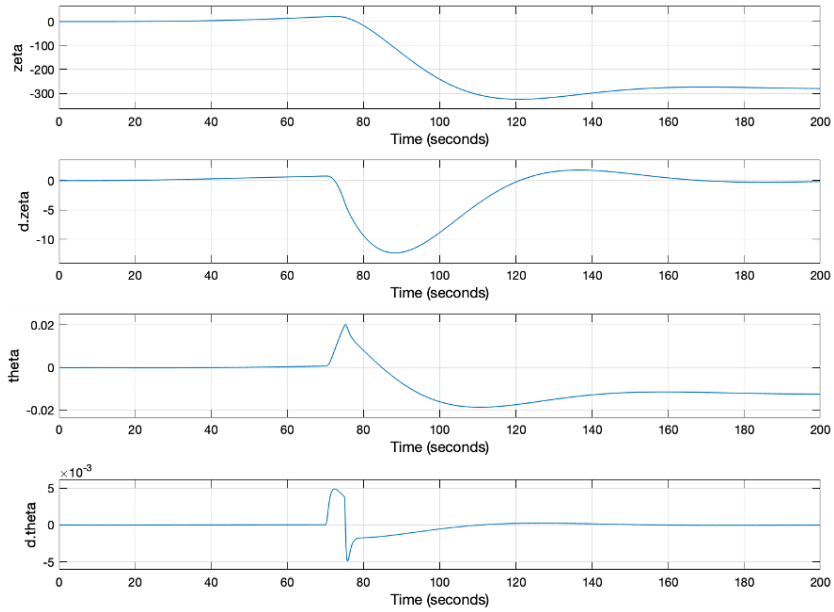

Figure 39: Test 1- Responses to manual pole placement

Fig. 39 shows the responses obtained are really slow, especially with respect to drift. The gains for drift and drift rate are then modified as

K_{P_z}	K_{D_z}	K_{P_θ}	K_{D_θ}	z_{max}	β	Aero GM	Rigid PM	Rigid GM
-0,0001	-0,0001	1,7	0,9	-279,7	-0,3956	6,81	58,3	27,2
-0,0003	**-0,005**	1,7	0,9	-93,3	-0,4069	6,12	56,1	27,4
-0,0008	-0,005	1,7	0,9	-35,02	-0,407	5,78	56,2	27,4

and its corresponding response becomes

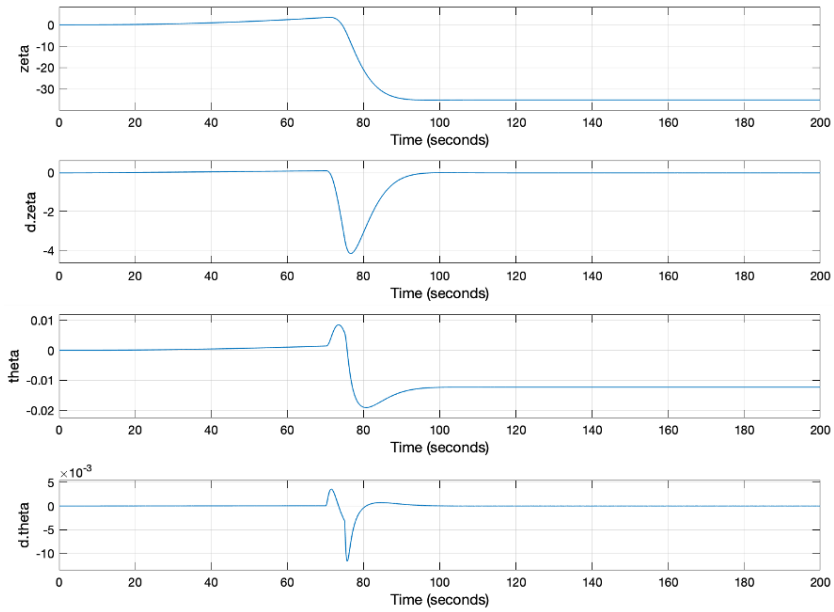

Figure 40: Test 2- Responses to manual pole placement

In this way, the response is much quicker as shown in Fig. 40.

However, stability has been jeopardized a bit, seen in the first row of the below table. To solve the problem, pitch gains are also modified.

K_{P_z}	K_{D_z}	K_{P_θ}	K_{D_θ}	z_{max}	β	Aero GM	Rigid PM	Rigid GM
-0,0008	-0,005	1,7	0,9	-35,02	-0,407	5,78	56,2	27,4
-0,0008	-0,005	1,7	**1**	-35,02	-0,4072	5,84	61	26,5
-0,0008	-0,005	1,7	**1,2**	-35,02	-0,4072	5,89	67,5	25
-0,0008	-0,005	1,7	**1,5**	-35,02	-0,4071	5,9	72,2	23,1
-0,0008	-0,005	1,7	**1,6**	-35,02	-0,4072	5,89	73	22,5
-0,0008	-0,005	**1,8**	1,5	-36,56	-0,4072	6,44	71,6	23

The final response is shown in Fig. 41.

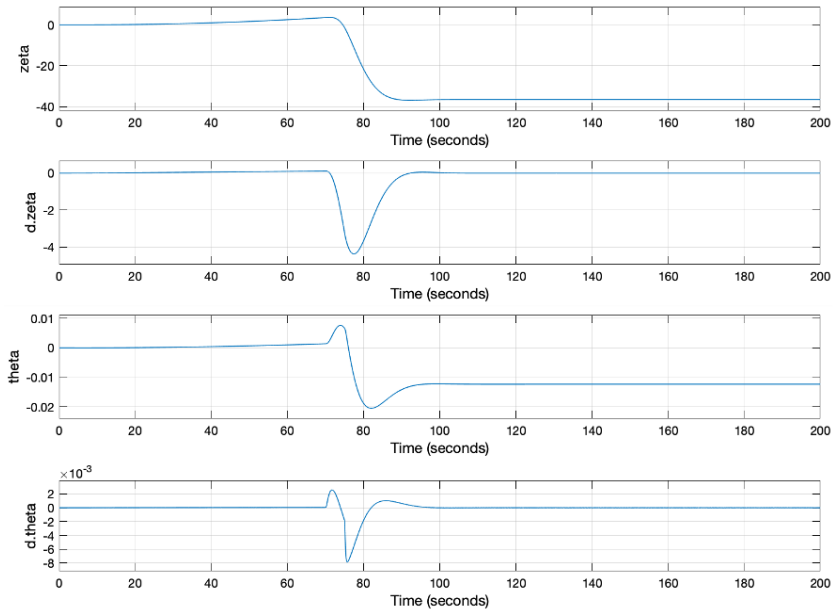

Figure 41: Test 3- Responses to manual pole placement

It has been managed to manually find a controller inside stability and performance requirements and improving the time response.

A.2 LQR gain search

In order to find the optimal **Q** and **R** matrices, these are first defined as

$$\mathbf{Q} = \begin{bmatrix} q_1 & 0 & 0 & 0 \\ 0 & q_2 & 0 & 0 \\ 0 & 0 & q_3 & 0 \\ 0 & 0 & 0 & q_4 \end{bmatrix}; \quad \mathbf{R} = r; \tag{53}$$

In the same way than in Annex A.1, all tests are obtained from the simulation of the system (Fig. 12) and done with the wind model 2 as input.

First, it is analysed the specific function of each element. Starting from all values equal to 1, they are then modified individually and their side effect is interpreted.

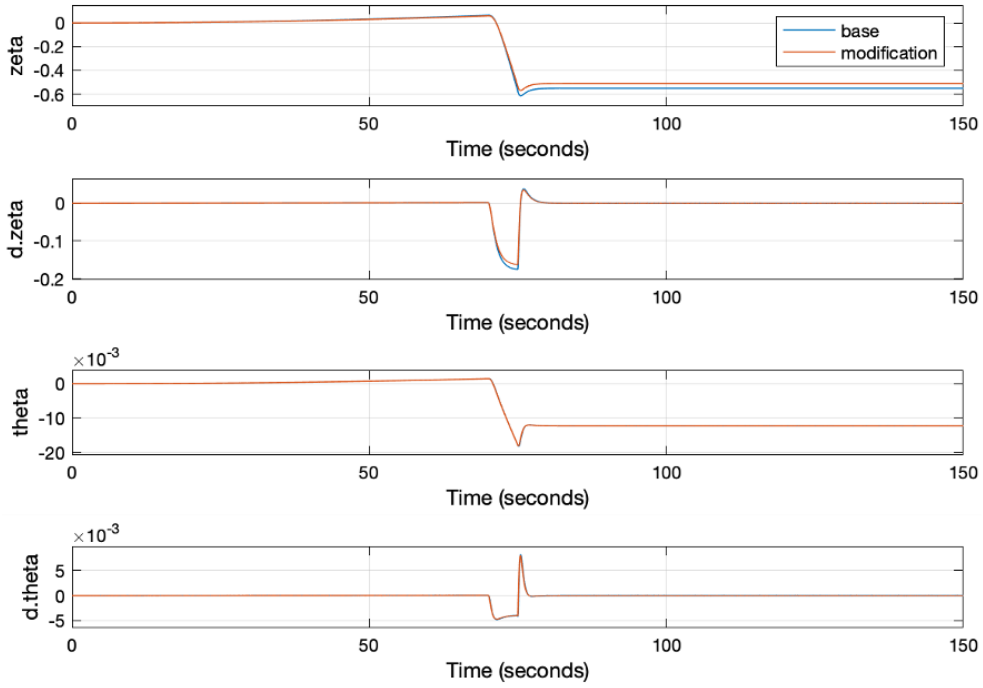

Figure 42: LQR tests for $r = 1$ (blue) and $r = 0.1$ (orange)

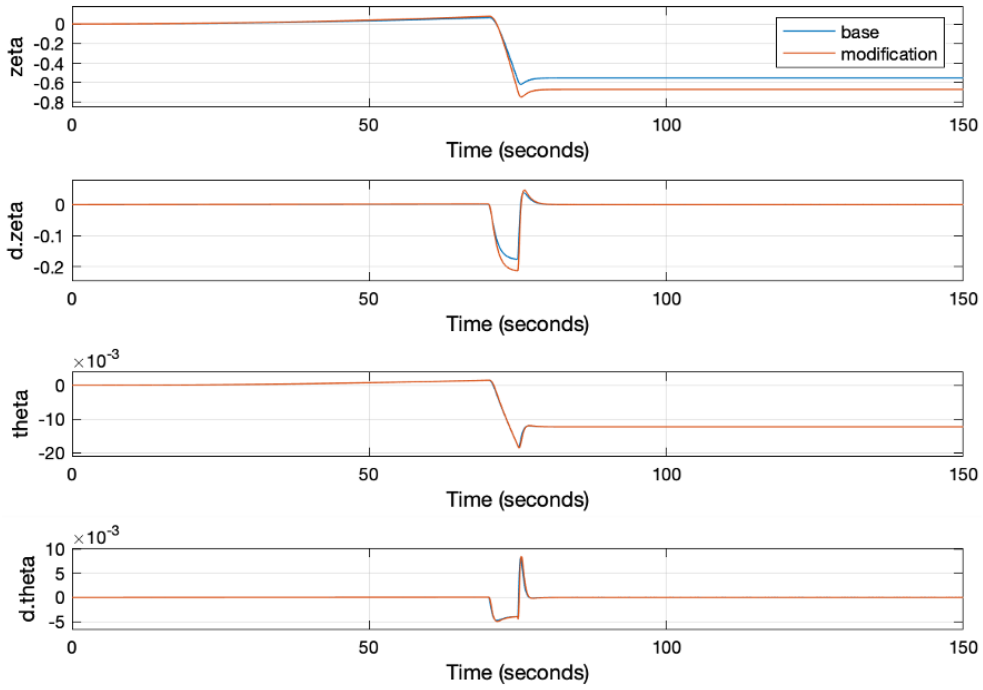

Figure 43: LQR tests for $r = 1$ (blue) and $r = 10$ (orange)

From Fig. 42 it is seen that, decreasing the value of r, the absolute value of drift is decreased with smaller overshoot although higher time response. The opposite effect than in Fig. 43, where r is increased.

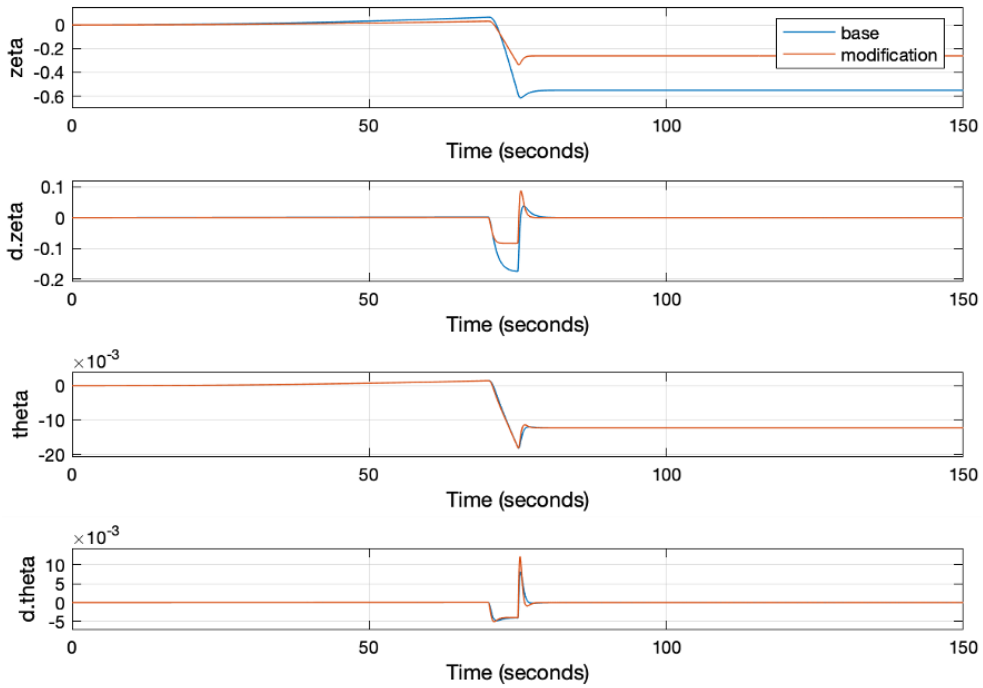

Figure 44: LQR tests for $q_1 = 1$ (blue) and $q_1 = 10$ (orange)

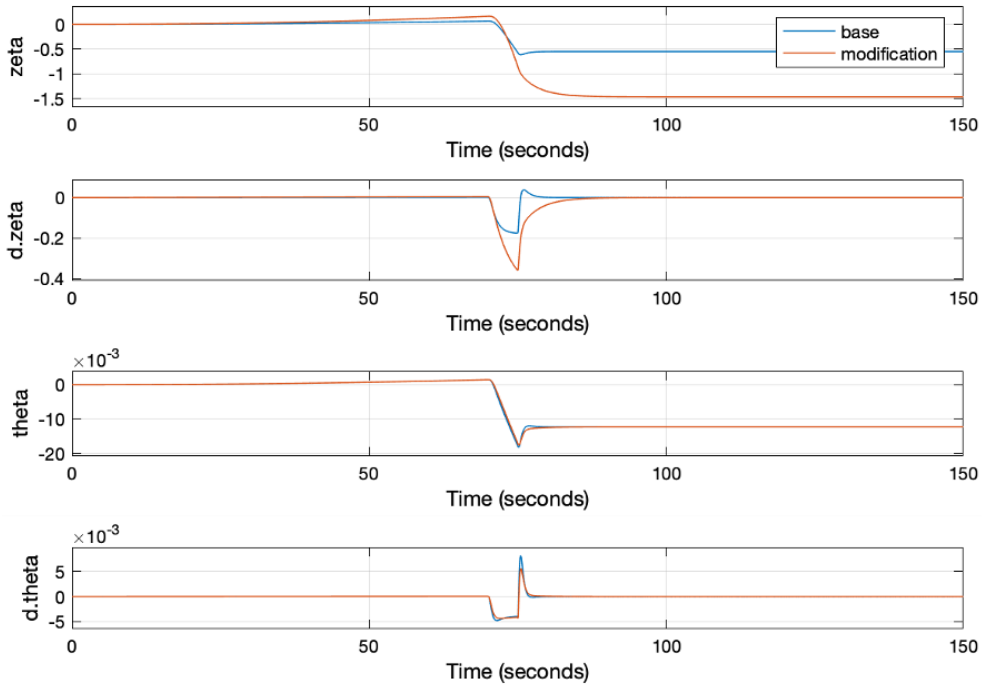

Figure 45: LQR tests for $q_1 = 1$ (blue) and $q_1 = 0.1$ (orange)

From Fig. 44 and Fig. 45 it is shown that, increasing q_1, the absolute value of drift is decreased with smaller time response although higher overshoot.

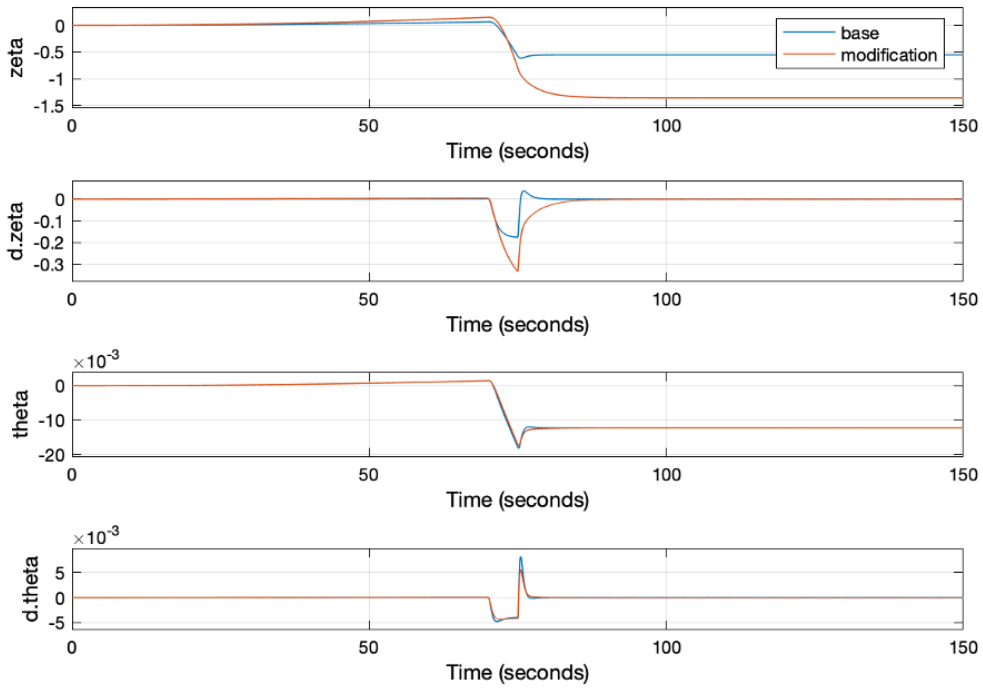

Figure 46: LQR tests for $q_2 = 1$ (blue) and $q_2 = 10$ (orange)

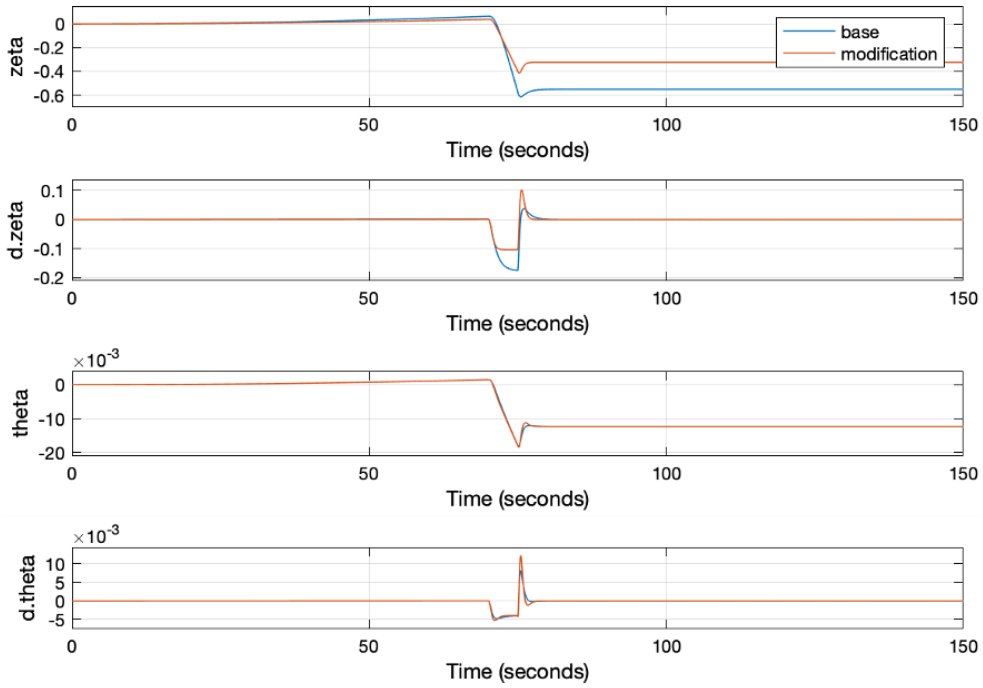

Figure 47: LQR tests for $q_2 = 1$ (blue) and $q_2 = 0.1$ (orange)

Fig. 46 and Fig. 47 state that, contrary to the latter case, the absolute value of drift is decreased with smaller time response although higher overshoot for a smaller value of q_2.

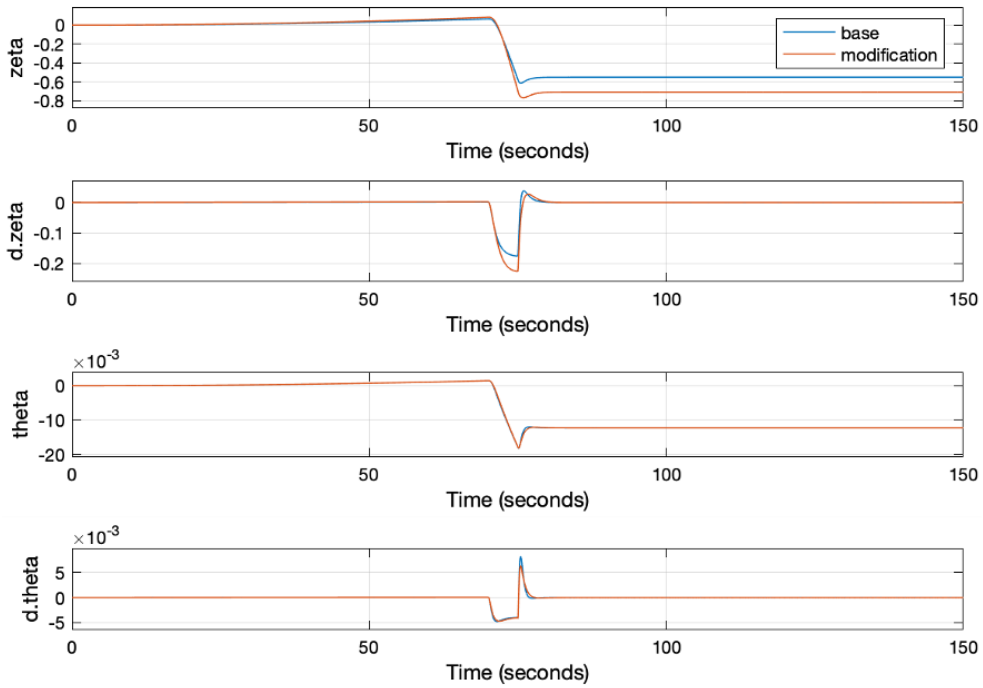

Figure 48: LQR tests for $q_3 = 1$ (blue) and $q_3 = 1000$ (orange)

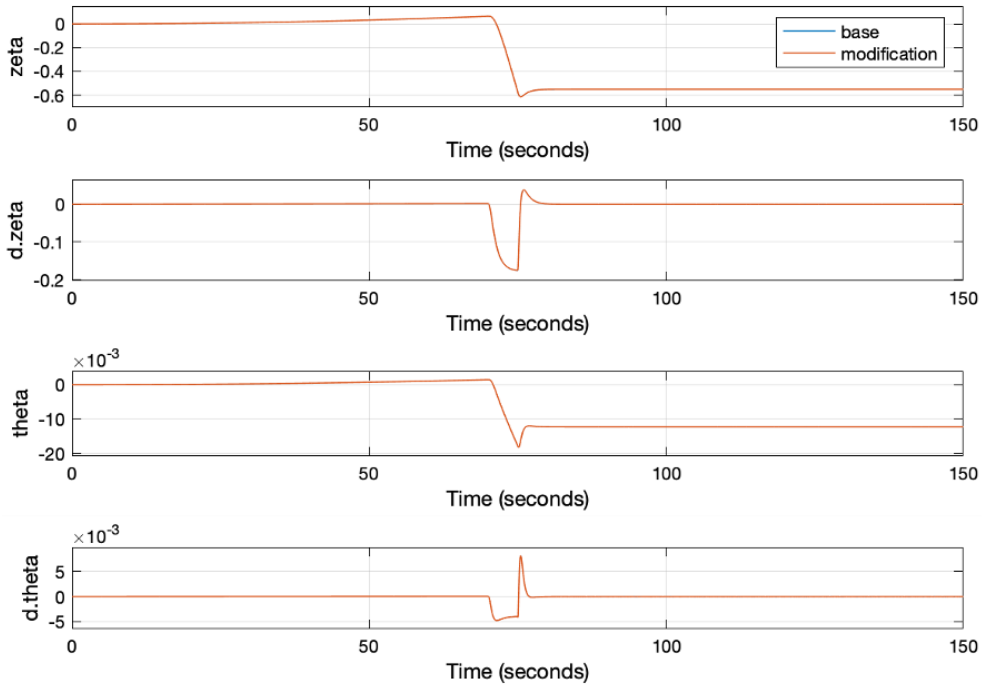

Figure 49: LQR tests for $q_3 = 1$ (blue) and $q_3 = 0.001$ (orange)

Fig. 48 illustrates that the absolute value of drift can be increased with a quite high value of q_3, whilst Fig. 49 shows that decreasing this value, there is no change.

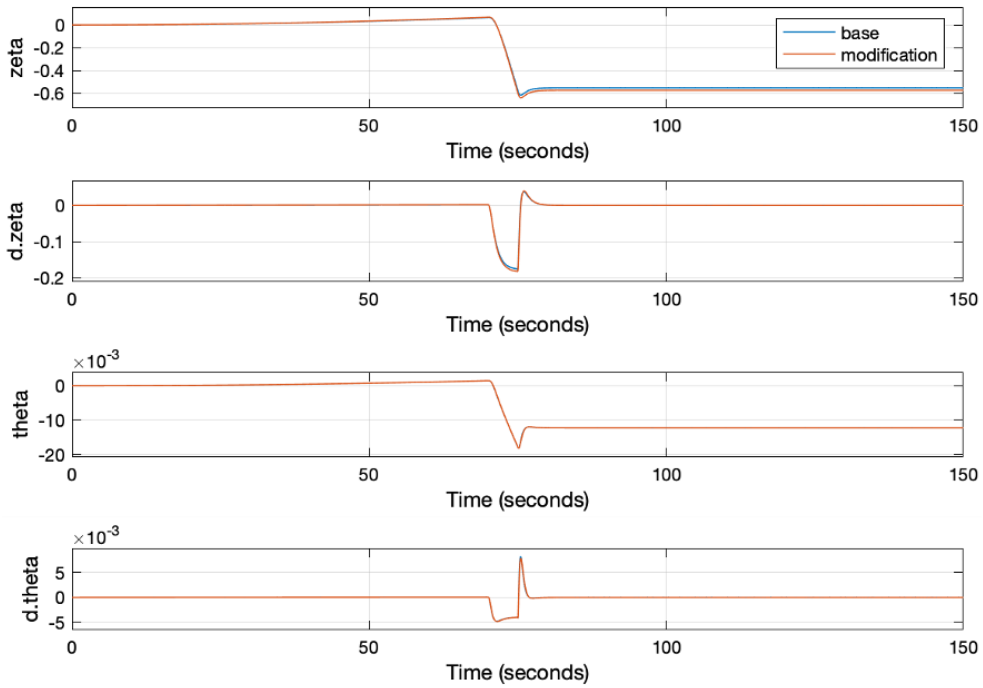

Figure 50: LQR tests for $q_4 = 1$ (blue) and $q_4 = 10$ (orange)

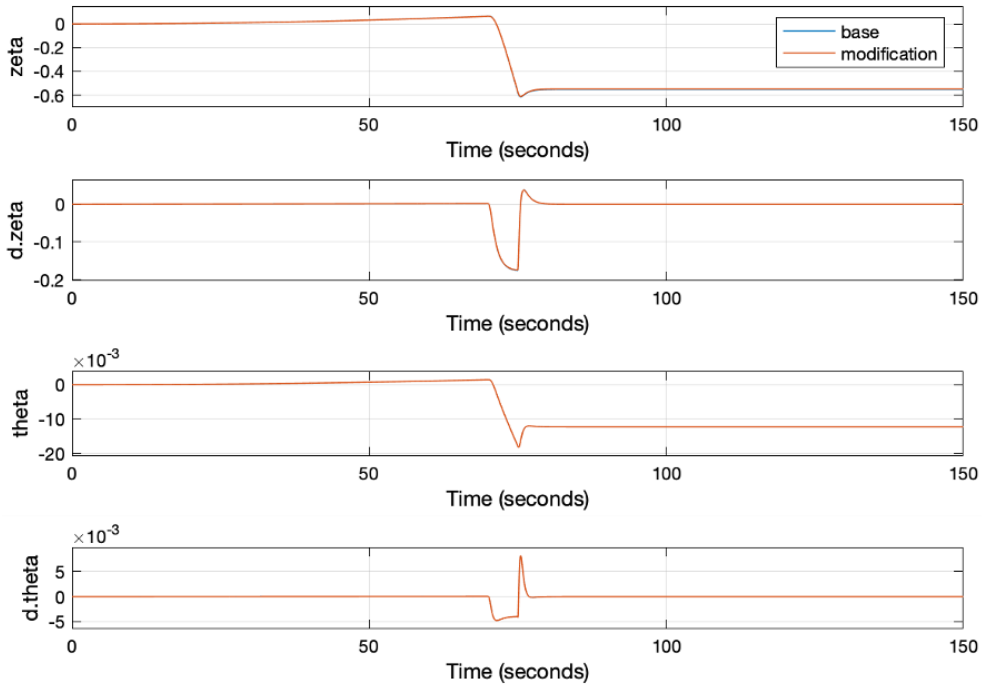

Figure 51: LQR tests for $q_4 = 1$ (blue) and $q_4 = 0.001$ (orange)

Fig. 50 and Fig. 51 have a similar response to the previous case, where increasing q_4, the absolute value of drift can be increased, although decreasing it has no effect on the response.

As an overview, changing the specified values of **Q** and **R** matrices only have an effect on drift and drift rate as the pitch angle has maintained unaltered in the whole process.

Regarding stability, it is also studied for the desired modifications of the values. This is, for a decreasing r and q_2 and an increasing q_1 while q_3 and q_4 will remain equal to 1.

R	Q1	Q2	Q3	Q4	Aero GM	Rigid PM	Rigid GM
1	1	1	1	1	18,9	42,9	9,57
0,1	1	1	1	1	27	5,19	1,09
0,01	1	1	1	1	36,2	-31,1	-8,35
1	**5**	1	1	1	17,5	40,3	9,06
1	**10**	1	1	1	16,8	38,4	8,7
1	**100**	1	1	1	15,4	27,6	6,52
1	1	**0,1**	1	1	12,3	49,5	14,6
1	1	**0,01**	1	1	10,2	49	16
1	1	**0,001**	1	1	9,87	48,9	16,2
1	1	**0,0001**	1	1	9,84	48,9	16,2

Considering the best combination with regard to both performance and stability, it is set

$$\mathbf{Q} = \begin{bmatrix} 5 & 0 & 0 & 0 \\ 0 & 0.01 & 0 & 0 \\ 0 & 0 & 1 & 0 \\ 0 & 0 & 0 & 1 \end{bmatrix}; \quad \mathbf{R} = 0.1; \tag{54}$$

Fig. 52 plots the Aero GM at 14 dB, Rigid PM at 34.2 deg and Rigid GM at 8.52 dB.

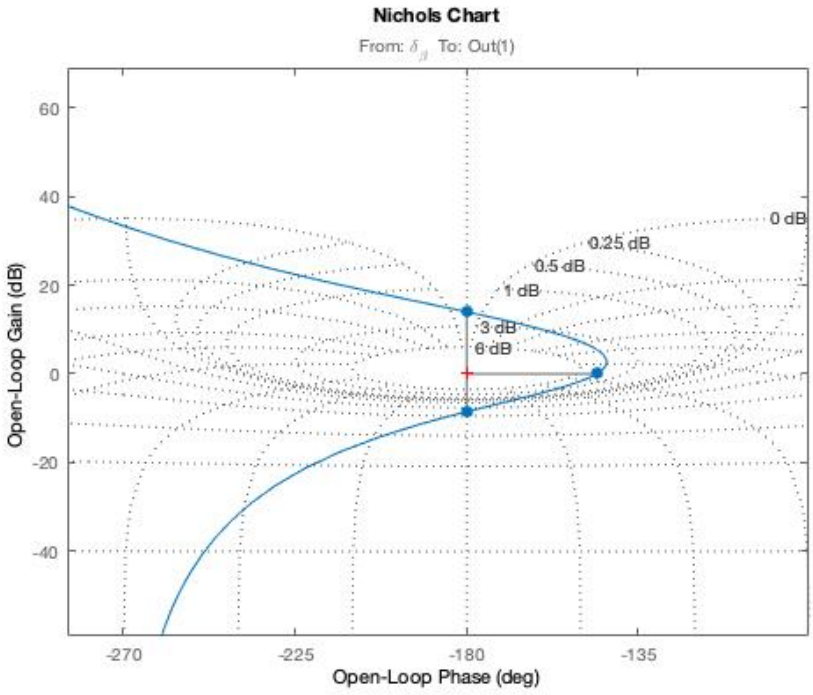

Figure 52: Nichols plot for final LQR controller

And the performance for this combination results in

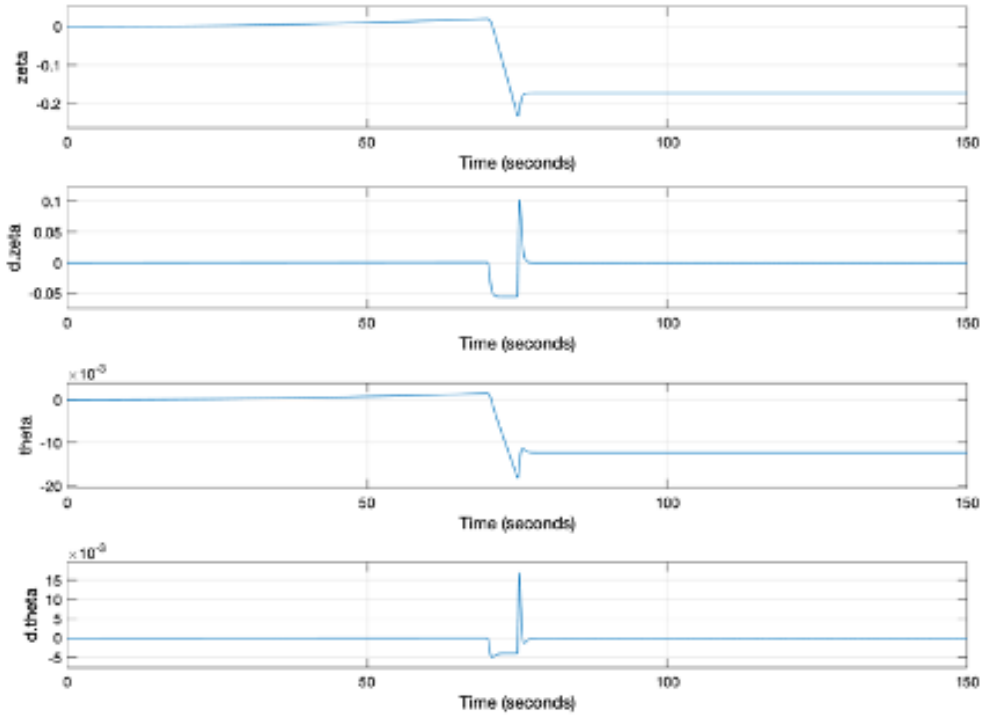

Figure 53: Responses plot for final LQR controller